Bioactive Materials 46 (2025) 365–385

Contents lists available at ScienceDirect

Bioactive Materials

journal homepage: www.keaipublishing.com/en/journals/bioactive-materials

3D bio-printed proteinaceous bioactive scaffold loaded with dual growth factor enhanced chondrogenesis and in situ cartilage regeneration

Prayas Chakma Shanto [a], Seongsu Park [a], Md Abdullah Al Fahad [a], Myeongki Park [a], Byong-Taek Lee [a,b,*]

[a] Department of Regenerative Medicine, College of Medicine, Soonchunhyang University, Cheonan, Republic of Korea
[b] Institute of Tissue Regeneration, Soonchunhyang University, Cheonan, Republic of Korea

ARTICLE INFO

Keywords:
3D bioprinting
dECM
TOCN
TGF-β1/FGF-18
Cartilage regeneration

ABSTRACT

Articular cartilage has a limited self-healing capacity, leading to joint degeneration and osteoarthritis over time. Therefore, bioactive scaffolds are gaining attention as a promising approach to regenerating and repairing damaged articular cartilage through tissue engineering. In this study, we reported on a novel 3D bio-printed proteinaceous bioactive scaffolds combined with natural porcine cancellous bone dECM, tempo-oxidized cellulose nanofiber (TOCN), and alginate carriers for TGF-β1, FGF-18, and ADSCs to repair cartilage defects. The characterization results demonstrate that the 3D scaffolds are physically stable and facilitate a controlled dual release of TGF-β1 and FGF-18. Moreover, the key biological proteins within the bioactive scaffold actively interact with the biological systems to create a favorable microenvironment for cartilage regeneration. Importantly, the *in vitro*, *in vivo*, and in silico simulation showed that the scaffolds promote stem cell recruitment, migration, proliferation, and ECM deposition, and synergistic effects of TGF-β1/FGF-18 with the bioactive scaffolds significantly regulate stem cell chondrogenesis by activating the PI3K/AKT and TGFβ1/Smad4 signaling pathways. After implantation, the proteinaceous bioactive scaffold led to the regeneration of mechanically robust, full-thickness cartilage tissue that closely resembles native cartilage. Thus, these findings may provide a promising approach for regulating stem cell chondrogenesis and treating in situ cartilage regeneration.

1. Introduction

Articular cartilage (AC) is an avascular connective tissue with unique properties, including toughness and a viscoelastic nature, that makes it essential for load-bearing and providing supportive lubrication during joint movement [1,2]. However, defects in articular cartilage, whether from traumatic injuries, chronic inflammation, or aging, pose significant clinical challenges. These defects can lead to severe joint pain, restricted movement, and even permanent joint disability. Furthermore, untreated cartilage damage may allow small lesions to progress, potentially leading to serious degenerative conditions such as osteoarthritis (OA) [3–7]. The treatment of this cartilage damage presents a formidable challenge and remains a primary concern in the clinical field due to the limited self-healing capability of the cartilage [8]. Currently, it affects over 303 million people globally, placing a substantial physical and psychological burden on patients, particularly among older adults [9]. The treatment strategies for cartilage damage and restoring natural functions include autologous chondrocyte implantation, microfracture, cartilage transplantation, and various medications [10,11]. However, these treatments may lead to significant tissue injury over the long term, which may lead to arthroplasty or total joint replacement. Therefore, further surgical procedures could be highly expensive for most of the patients suffering from chronic OA.

With emerging technology and significant advancements in engineering and medicine, the tissue engineering approach has been recognized as a promising method for cartilage tissue regeneration [12,13]. Recently, injectable hydrogel-based systems have been widely investigated for cartilage regeneration due to their similarity to ECM properties [14–16]. Furthermore, studies have demonstrated that hydrogel loaded with mesenchymal stem cells (MSCs) effectively promotes cell proliferation and exhibits therapeutic effects on cartilage regeneration [17–21]. However, despite their potential to facilitate minimally invasive surgery, along with simple stem cell and drug-loading capabilities, these systems exhibit technique several

* Corresponding author. Department of Regenerative Medicine, College of Medicine, Soonchunhyang University, Cheonan, Republic of Korea.
E-mail address: lbt@sch.ac.kr (B.-T. Lee).

https://doi.org/10.1016/j.bioactmat.2024.12.021
Received 13 September 2024; Received in revised form 26 November 2024; Accepted 19 December 2024

drawbacks, including insufficient mechanical strength, challenges in maintaining structural integrity to mimic cartilage defects, and rapid degradation rates [22–24]. Therefore, 3D bioprinting technology has been employed to replicate the complex shape and structure of the cartilage defects [25–30]. Some synthetic polymer-based scaffolds are also utilized for cartilage tissue regeneration using various fabrication techniques. However, still these scaffolds face challenges in repairing cartilage damage due to slow degradation rates, high infection rates, and foreign body reactions [31]. In contrast, naturally occurring biomaterials such as silk, collagen, and hyaluronic acid match the biological properties of cartilage, although they exhibit poor mechanical strength [32,33]. The mechanical properties and structural integrity are crucial for promoting stem cell differentiation and cartilage regeneration [29,34]. Therefore, the development of novel 3D bio-printed stem cell-laden bioactive scaffolds for cartilage repair aims to provide the following advantages: mimicking the shape and size of cartilage defects, enabling minimally invasive surgery, achieving similar mechanical strength to the native cartilage, and facilitating stem cell recruitment, migration, proliferation, and chondrogenic differentiation.

Recent studies have shown that the decellularized cancellous bone extracellular matrix (dECM) contains key biological proteins crucial for regulating a favorable microenvironment for stem cell chondrogenesis [35–37]. Consequently, dECM represents a promising source for providing the native microenvironment necessary for cartilage regeneration. Furthermore, tempo-oxidized cellulose nanofiber (TOCN), a plant-derived cellulose nanofiber, is recognized as an exceptionally biocompatible material for tissue engineering [36]. Integrating TOCN with the dECM hydrogel has significantly enhanced the viscosity and maintained 3D shape integrity during bioprinting [38]. Despite offering excellent biocompatibility and stability, this combination has relatively lower mechanical strength and 3D shape integrity compared to other synthetic hydrogels such as polycaprolactone (PCL), polyethylene glycol (PEG), and polylactic acid (PLA) [39–41]. Therefore, Sodium alginate (SA) was incorporated into this combination to resolve these shortcomings. Sodium alginate (SA), a natural polysaccharide, exhibits a rapid cross-linking capability with calcium chloride that enhances mechanical properties and preserves structural fidelity throughout 3D printing processes [42,43]. Additionally, studies reported that rabbit adipose-derived stem cells (ADSCs) are effective in cell-based therapy for OA due to their rapid proliferation, differentiation, and minor immunological rejection [44]. In situ tissue regeneration is facilitated by using functional bioactive scaffolds combined with stem cells, which support the restoration process by delivering bioactive signals. Hence, to further enhance cell proliferation, migration, and chondrogenic differentiation, this research introduced the difunctional dual-release of transforming growth factor (TGF-β1), and fibroblast growth factors (FGF-18). TGF-β1, a well-recognized chondrogenic growth factor, interacts with the TGF-β R2 receptor to activate downstream molecules such as Smad4 [45]. Some research has demonstrated that TGF-β1 significantly promotes chondrogenic differentiation with ADSCs by enhancing extracellular matrix synthesis and chondrocyte maturation [46–50]. In combination with BMP-2, TGF-β1 synergistically enhances chondrogenic differentiation of adipose-derived stem cells while inhibiting osteogenic differentiation [51]. Additionally, FGF-18 has been identified as influential in stimulating stem cell proliferation, inhibiting OA, and promoting cartilage regeneration through the activation of the PI3K/AKT signaling pathway. Currently, FGF-18 also known as sprifermin, is undergoing clinical trials for cartilage injury repair [52–54]. Studies have shown that FGF-18 signaling through FGFR3 enhances cartilage matrix production and suppresses chondrocyte proliferation in mesenchymal cells [52]. FGF-18 has been found to stimulate earlier chondrogenic differentiation, increase extracellular matrix production, and delay terminal hypertrophy compared to FGF-2 [55,56].

In this study, we present a novel proteinaceous bioactive scaffold loaded with difunctional dual growth factor FGF-18/TGF-β1 and stem cell by 3D bio-printing technology for cartilage tissue regeneration. We hypothesized that the complex structure of the 3D bio-printed DTSTF scaffold (mentioned in Table 1) would facilitate minimally invasive implantation and closely resemble the cartilage defect, thereby mimicking the native microenvironment. Furthermore, we assume that the dual release of TGF-β1 and FGF-18, along with the key biological proteins from the bioactive DTSTF scaffold could activate the PI3K/AKT and TGFβ1/Smad4 signaling pathways and enhance ADSCs recruitment, proliferation, migration, and effective chondrogenic differentiation. The key novel aspect of our study is that the biologically inspired, proteinaceous 3D-printed scaffold is uniquely integrated with dual growth factors to mimic the environment of natural cartilage. Notably, there is currently no comprehensive protein profile characterization of porcine cancellous bone ECM available in the literature, making its use for cartilage regeneration quite uncommon. To address this gap, we largely analyzed the protein profile of decellularized porcine cancellous bone ECM (dECM), focusing on key structural and bioactive proteins essential for chondrogenesis and regenerative potential as a scaffold in cartilage tissue engineering. While many research studies use traditional growth-factor-based strategies, we developed a 3D-printed, proteinaceous scaffold that combines porcine cancellous bone decellularized extracellular matrix (dECM), nanocellulose (TOCN), and dual growth factors (FGF-18 and TGF-β1) within an adipose-derived stem cell (ADSCs) matrix. This integration achieves a highly bioactive microenvironment that not only supports cellular adhesion, proliferation, and differentiation but also mimics native cartilage structures with a high degree of biological fidelity (Scheme 1). Thus, the proteinaceous bioactive scaffold could modulate a favorable chondrogenic microenvironment and could be a promising approach for mechanically stable in situ cartilage regeneration.

2. Results and discussion

2.1. Characterization and proteomics analysis of decellularized extracellular matrix

dECM is a promising biomaterial source and possesses essential biological components crucial for cartilage regeneration [57]. To determine the optimal decellularization method, histological analyses, and protein quantification were performed to verify the dECM. Importantly, the goal of the decellularization process is to completely remove cells from the tissue while retaining the critical biological proteins and components. Results depicted in Fig. S1A, including the H&E, and DAPI staining, confirm that the cells were completely removed after the decellularization process compared to the native ECM. Additionally, the SEM images revealed evident surface morphology differences between the native and decellularized bone matrix. Furthermore, DNA quantification demonstrated a significant reduction after the decellularization process, with only 3.065 ng/mg of DNA content remaining, as shown in Fig. S1B. Both glycosaminoglycans (GAGs) and collagen were well preserved, with Figs. S1C and S1D indicating that 0.215 μg/mg and 114.2 μg/mg of total GAGs and collagen remained post-decellularization, respectively. These findings confirm the effectiveness of the decellularization process, achieved by employing a combination of enzymes and chelating agents.

Furthermore, to assess the proteinaceous bioactive scaffold and

Table 1
Composition of different ADSCs-laden bio-inks.

Sample	dECM (D) (%)	TOCN (T) (%)	Sodium Alginate (S) (mg/ml)	TGF-β1 (T) (ng/ml)	FGF-18 (F) (ng/ml)
DTS	1	1	40	0	0
DTST	1	1	40	10	0
DTSF	1	1	40	0	20
DTSTF	1	1	40	10	20

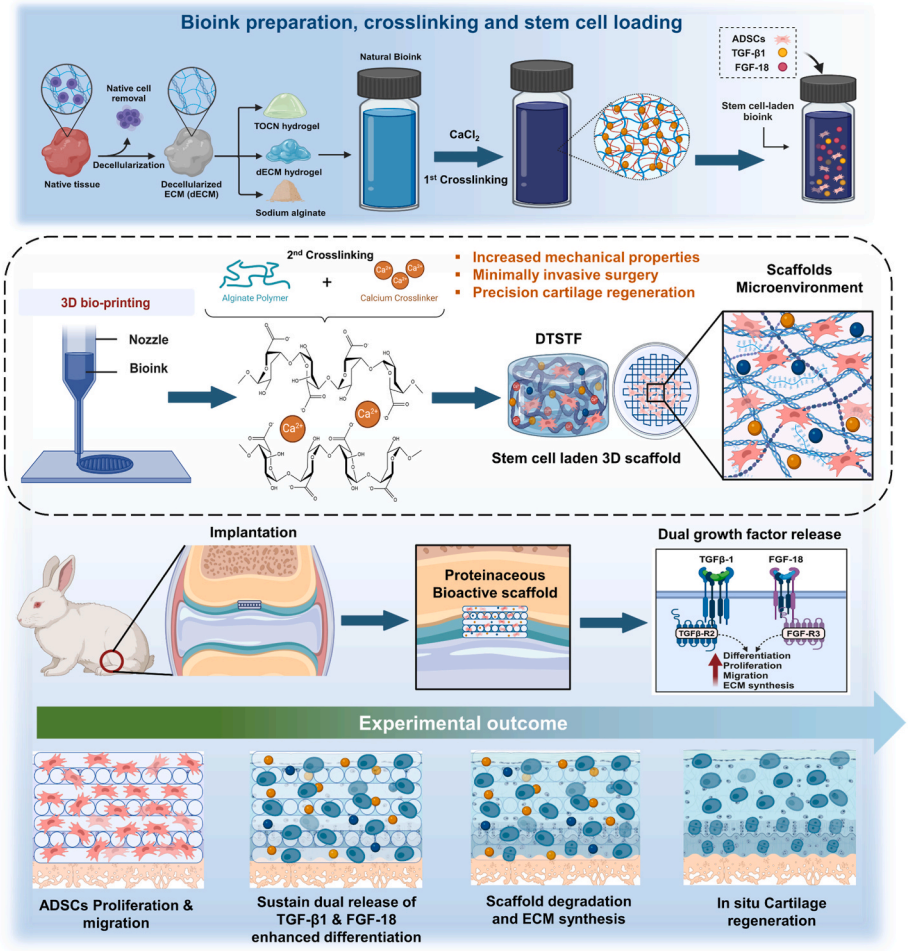

Scheme 1. Schematic demonstration of FGF-18/TGF-β1 functionalized dual-factor releasing 3D bio-printed stem cell-laden bioactive scaffolds for in situ cartilage regeneration.

determine whether the key biological proteins increased or decreased post-decellularization, and to compare the protein composition between native and decellularized ECM, liquid chromatography-tandem mass spectrometry (LC-MS/MS) was used in this research. In Fig. 1A, LC-MS/MS proteomic analysis identified a total of 18.32 % up-significant proteins, 33.33 % down-significant proteins, and 48.35 % non-specific proteins in the dECM compared to the native. All up-significant and down-significant proteins in decell/native were illustrated by scatter plot in Fig. 1B. Additionally, the results (Fig. 1C–S1E, F, & G) revealed that proteins associated with chondrocyte differentiation, cartilage development, proteoglycan, extracellular matrix, immune response, and inflammatory response were up-significant after decellularization, while proteins related to cell migration and cell differentiation were predominantly down-significant. The heatmap of differently expressed proteins between decell and native (Fig. 1D) indicated that most of the highly expressed proteins in the listed molecules were related to core ECM organization and chondrogenesis. Consequently, radar plots and gene plot analyses were conducted to further elucidate their expression profiles. In Figs. S1H and I, it was demonstrated that the core ECM organization proteins in decell, such as COL1A1, COL1A2, COL2A1, and COL12A1 were highly expressed, with relative abundance percentages of 93.03 %, 95.57 %, 93.15 %, and 90.98 % respectively. The relative abundance percentages related to the core ECM proteins are detailed in Table S1. Moreover, the formal analysis of functional protein association networks in Fig. 1E showed extensive physical and functional interconnections among core ECM proteins in their gene neighborhoods, with collagens, and tropocollagens factors being the most interconnected molecules in the networks. Specifically, COL1A1, COL1A2, and COL2A1 were notably interconnected with the Collagen alpha-2(V) chain (COL5A2) and Aggrecan core protein (ACAN). Collagens, being the most abundant matrix proteins in the ECM, contribute significantly to the overall stiffness of cartilage [58]. In contrast, the radar plot and gene plot analysis of cell migration (Figs. S2A and B) and cell differentiation (Fig. 1H & S2C) revealed a significant loss in protein abundance following decellularization. All up-significant and down-significant proteins related to cell differentiation and cell migration, along with their functional association networks, are presented in Figures S3 A, B, C & D. The relative abundance percentages provided in Tables S2 and S3 further confirmed the reduction in proteins associated with cell migration and proliferation post decellularization. However, proteins related to cartilage development and chondrocyte differentiation were preserved and enhanced after decellularization, as evidenced in Fig. 1I–S2D, and Tables S4 and S5. Additionally, up-significant proteins and their functional association networks, illustrated in Figs. S3E and F, demonstrated that all the proteins were strongly interconnected both physically and functionally to initiate cartilage development. Another significant advantage of utilizing cancellous bone ECM is the potential reduction in immune rejection and the enhancement of the inflammatory response, as demonstrated in Figures S4 A, B, C & D. These findings indicated that the functional proteins and their interconnected networks, including Vitronectin (VTN), Keratin, type II cytoskeletal 1 (KRT1), Prothrombin (F2), C-reactive protein (CRP), and Alpha-2-HS-glycoprotein (AHSG), play crucial roles in modulating immune rejection and enhancing the inflammatory response upon

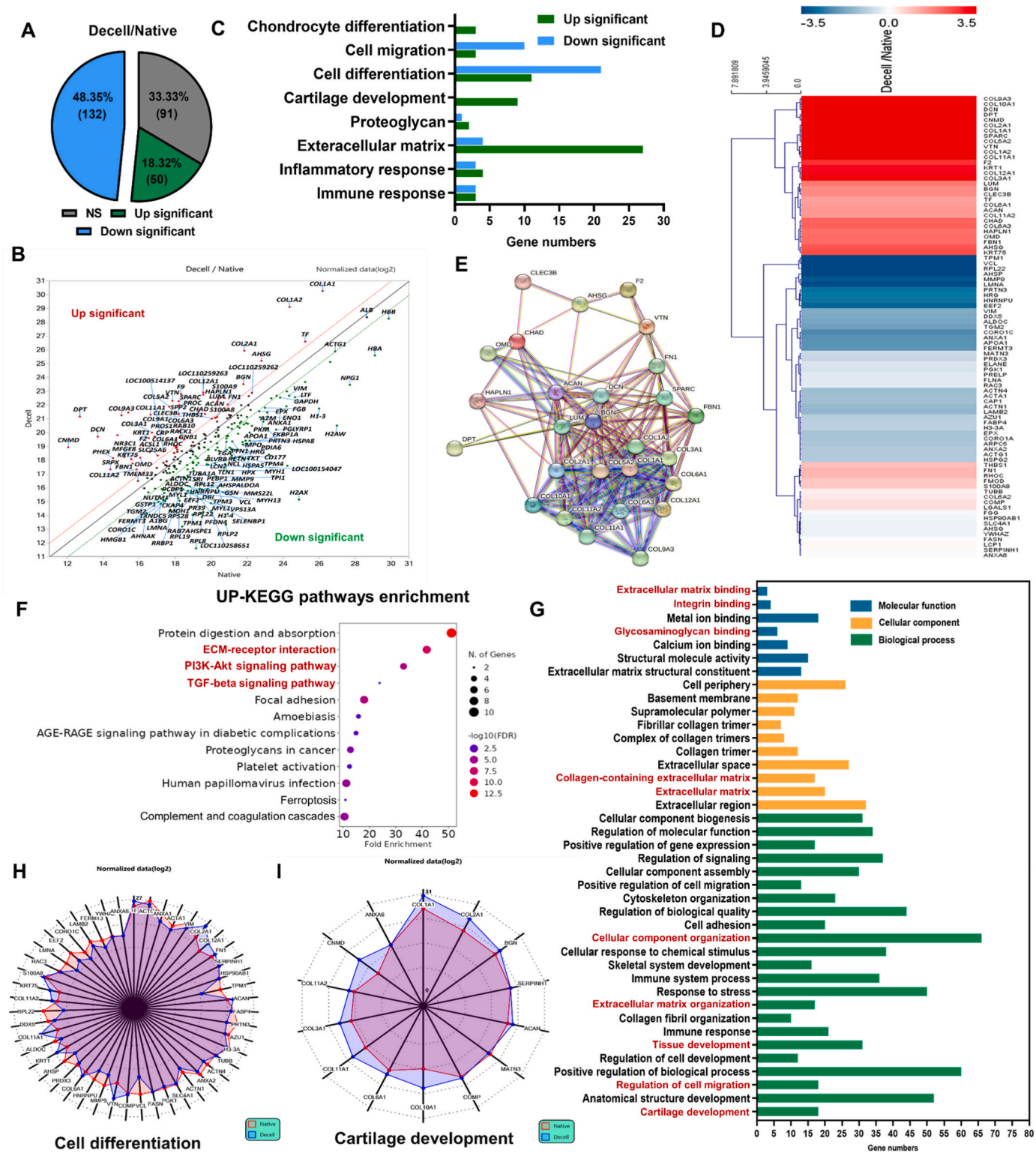

Fig. 1. (A) Significant profile of differentially expressed proteins after LC-MS/MS analysis of decell/native. (B) Up-significant and down-significant proteins present in decellularized ECM (C) A significant number of proteins related to cartilage regeneration are present in decellularized ECM. (D) Heatmaps of differentially expressed proteins comparison between decell/native. (E) Functional protein association networks of ECM core proteins were established using the STRING database. (F) UP-KEGG pathway enrichment analysis identifying the abundance of differentially expressed proteins in biological categories comparison between decell/native. (G) Gene Ontology enrichment analysis of differentially expressed proteins between decell/native. Radar chart analysis for (H) cell differentiation-related proteins and (I) cartilage development-related proteins.

application.

Furthermore, the proteins identified by LC-MS/MS were further analyzed using the Kyoto Encyclopedia of Genes and Genomes (KEGG) pathway database. The results (Fig. 1F & S5A) demonstrated that most of the proteins with high fold enrichment percentages were associated with ECM-receptor interactions, P13-AKT signaling pathway, and TGFβ signaling pathway, all of which play a role in controlling environmental information processing. Several studies have confirmed that the molecular mechanisms underlying stem cell proliferation, migration, differentiation, and cartilage regeneration are regulated by the P13-AKT and TGFβ signaling pathways [59,60]. In addition, the results in Fig. S5B revealed that the down-regulated proteins in the pathways controlling gluconeogenesis, pentose phosphate pathway, and biosynthesis of amino acids contained high fold enrichment percentages.

The gene ontology enrichment analysis (Fig. 1G) indicated that most proteins are associated with the chondrogenic-related factors that activate the P13-AKT signaling pathway and TGF-beta signaling pathway for cartilage regeneration. Among these, proteins related to cartilage

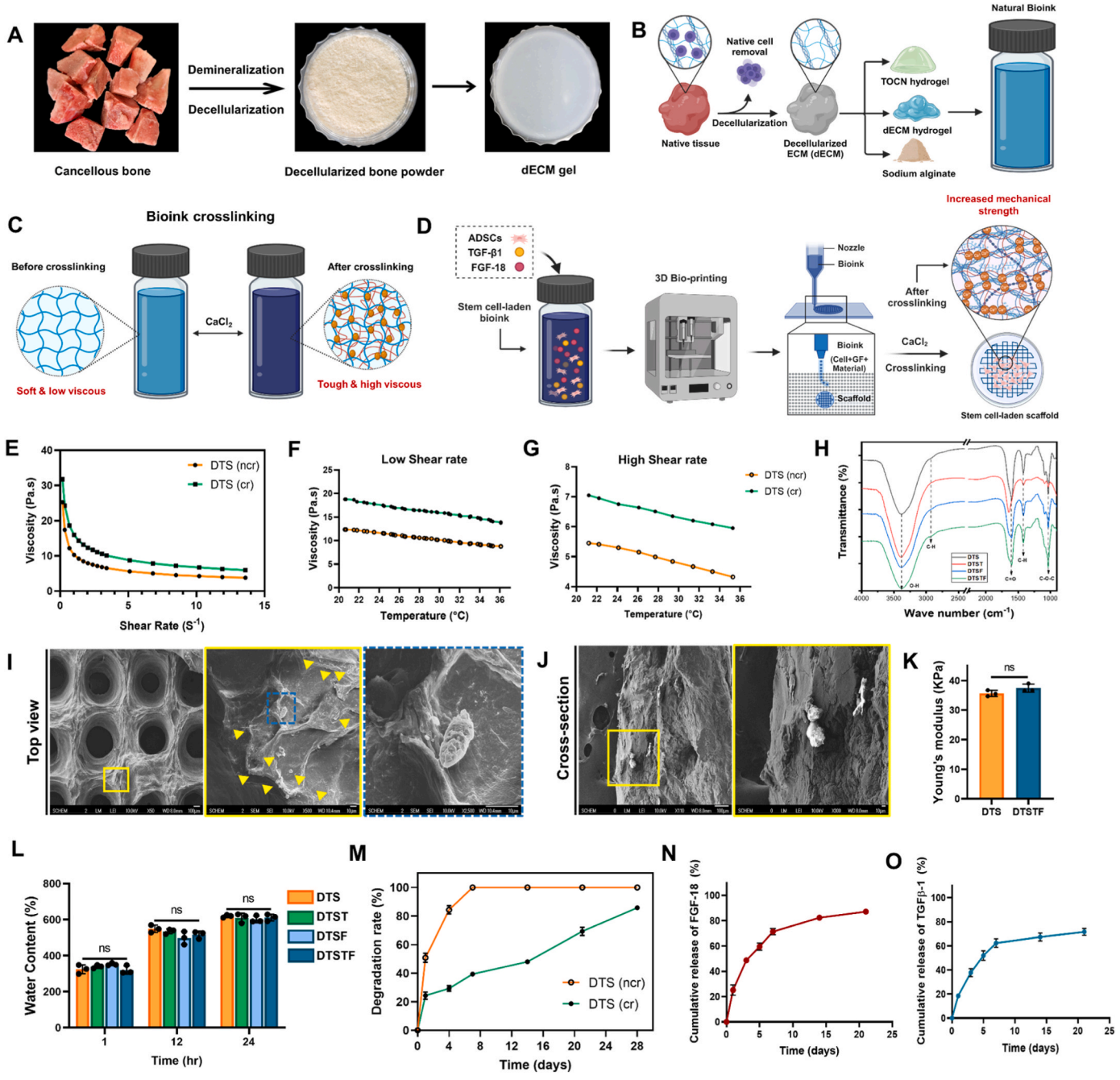

Fig. 2. (A) Optical images of the cancellous bone ECM decellularization procedure. (B) Schematic illustration of natural bio-ink preparation (C) Bio-ink partial crosslinking process with $CaCl_2$ solution (D) Schematic illustration of the stem cell-laden 3D bio-printing procedure. (E) The viscosity of the bio-ink before and after crosslinking. (F, G) Temperature sensitivity analysis of the bio-inks viscosity at low and high shear rates. (H) FTIR analysis (I) SEM images of the 3D bio-printed scaffolds after 24 h (Top view), taken in 50x, 500x and 2500x. (J) Cross-sectional SEM images (110x and 300x) for cell and surface morphology. (K) Young's modulus analysis from the slope of the stress-strain curve. (L) Water content behavior of the scaffolds after 1, 12, and 24 h of incubation. (M) Degradation rate of the samples DTS(ncr) and DTS(cr), without and with crosslinking respectively after 1, 4, 7, 14, 21, and 28 days of incubation. Cumulative release profile of (N) FGF-18 and (O) TGFβ-1. 3I Data are presented as mean ± SD.

development, regulation of cell migration, tissue development, extracellular matrix organization, cellular component organization, collagen-containing ECM, ECM binding, glycosaminoglycan binding, and integrin binding were highly implicated with cartilage regeneration. It was also determined that dECM has a significant potential to promote cartilage regeneration but may inhibit cell migration and differentiation due to a reduction in protein abundance following the decellularization process.

2.2. Fabrication, characterization, and in vitro drug release profile of 3D bio-printed stem cell-laden scaffolds

After decellularizing native cancellous bone ECM, a natural bio-ink composed of TOCN, dECM, and sodium alginate was prepared (Fig. 2A and B). However, the bio-ink should possess high viscoelastic behavior under high shear stress to increase the printability. If the appropriate viscoelastic property is achieved, the bio-ink would pass through the 3D bioprinting nozzle in a stable condition [61,62]. Therefore, in this work, we selected the optimized composition that has high viscoelastic properties and printability from our previously published study [36]. Moreover, studies showed that the incorporation of TOCN in the hydrogel significantly increased the viscoelastic properties and maintained the shape integrity during printing [36,63,64]. Thus, the viscosity results (Fig. S6) showed that bio-ink with TOCN has a high viscosity compared to without TOCN. Therefore, the high amount of TOCN in the bio-ink enhanced the printability, and the low amount of TOCN decreased the printability of the scaffold, which was already proved in our previous study [36]. Additionally, the partial crosslinking results of Fig. 2C also demonstrate that by introducing calcium ions into the bio-ink, the interconnections among multidimensional polymer chains were significantly strengthened, leading to a paste-like structure that promisingly increased the viscoelastic properties [65–67]. Consequently, the viscosity results (Fig. 2E) indicated that crosslinked bio-ink DTS (cr) viscosity increased to 31.75 Pa s, while the non-crosslinked DTS (ncr) reached 25.25 Pa s at a 0.17 S^{-1} shear rate. Additionally, the viscosity and rheological properties of the bio-ink could be influenced due to temperature sensitivity and shear thinning behavior. Therefore, a temperature sensitivity test was conducted to further verify the appropriate viscosity of the bio-ink according to the low and high shear rates. The results (Fig. 2F) revealed that at a low shear rate (0.17 S^{-1}) when the temperature increased from 20 to 37 °C, the viscosity decreased dramatically in both bio-ink and finally the viscosity dropped at 13.74 Pa s and 8.75 Pa s in DTS (cr) and DTS (ncr) respectively. Furthermore, the results (Fig. 2G) at a high shear rate (13.60 S^{-1}) both of the bio-ink viscosity dropped significantly by increasing the temperature up to 37 °C. The results showed 7.86 Pa s and 4.26 Pa s in DTS (cr) and DTS (ncr) respectively. Here, the bio-ink adhered to the common non-Newtonian fluids shear thinning theory, in which the viscosity decreases as the shear rate and temperature increase, maintaining excellent shape fidelity and continuous flow from the 3D bio-printing nozzle during printing [61,68,69]. Therefore, these findings suggested that partial crosslinking significantly increases the viscosity of bio-ink, rendering it highly suitable for 3D bio-printing. However, the bio-ink was still not configured to provide an optimal microenvironment for the stem cells to proliferate, migrate, and induce chondrogenic differentiation for mechanically dense cartilage regeneration. In this study, we introduced FGF-18 and TGF-β1 growth factors, along with ADSCs into the natural bio-ink to prepare a stem cell-laden bio-ink ideally suited for cartilage regeneration. Fig. 2D illustrates the 3D bio-printing process with stem cell-laden bio-ink used to fabricate a stable 3D scaffold. After 3D bio-printing, the 3D scaffold underwent further crosslinking with a calcium chloride solution to increase the mechanical properties of the scaffold. In this study, physical crosslinking was favored to enhance the mechanical properties since the 3D scaffold was loaded with stem cells and most of the reactions from physical crosslinking do not elicit any toxicity, unlike chemical crosslinking [70]. Here, crosslinking occurred, when water-soluble and charged polymers strongly bonded with ions of the opposite charge, transforming the hydrogel into a solid stable structure [67,71]. To prevent the possible formation of calcified cartilage due to the presence of an excess amount of calcium ions on the scaffold, it was washed thoroughly with sterile PBS. Furthermore, FTIR was performed to assess the functional groups of the 3D scaffolds. A total of 4 types of 3D scaffolds (DTS, DTST, DTSF, and DTSTF) were prepared for this study (Table 1), and their functional groups were analyzed. The results (Fig. 2H) displayed spectral bands at 3380 cm^{-1} corresponding to O-H, 2882 cm^{-1} corresponding to C-H, 1625 cm^{-1} corresponding to the carbonyl groups (C=O), 1400 cm^{-1} corresponding to C-H, and 1062 cm^{-1} corresponding to C-O-C stretching vibrations. All the absorption peaks were consistent across the samples and clearly signified the successful integration of the individual biomaterials into the samples. SEM observation was conducted on the 3D scaffold after 24 h of culture to examine the detailed surface morphology of the stem cell-laden scaffold. Fig. 2I showed that the surface of the scaffold was solid and uniformly structured post-crosslinking, indicating the strong mechanical properties of the scaffold. Moreover, the cells adeptly handled the pressure from the 3D bio-printing process and were uniformly distributed throughout the 3D scaffolds. The yellow arrowhead highlighted the cell distribution and cell morphology on the scaffold. Additionally, in Fig. 2J, the cross-sectional SEM images depicted that the cells were well distributed and maintained their proper morphology within the scaffold.

The mechanical strength of the scaffolds was further assessed to verify the effectiveness of the crosslinking process. In our previous study, we demonstrated that a higher concentration of TOCN together with ionic crosslinking using $CaCl_2$ markedly increased the mechanical strength of the scaffolds [36]. However, differences in composition could impact the elastic modulus of the samples. Therefore, according to Fig. 2K, Young's modulus results showed that the DTS had an elastic modulus of 35.65 ± 32.5 KPa, while the DTSTF exhibited an elastic modulus of 37.41 ± 73.2 KPa. Despite the incorporation of stem cells and growth factors, there was no significant difference in the mechanical strength between the samples. Additionally, the results further proved that the addition of TOCN and the incorporation of Ca^{2+} ions into the alginate-based scaffolds formed a stable network and a promising strategy to improve mechanical properties. The swelling behavior was also checked further to confirm the hydrophilic properties of the scaffolds. The swelling behavior is very crucial for facilitating cell migration, cell proliferation, and transferring the essential nutrients within the cells inside the scaffold structures [72]. The results presented in Fig. 2L & S7 indicated no significant differences in swelling properties among the samples after adding the growth factors. The scaffolds achieved the complete equilibrium state after 24 h and showed a swelling fraction of 17.66 %, 17.04 %, 17.28 %, and 17.51 % on DTS, DTST, DTSF, and DTSTF respectively. The results indicated the scaffolds did not exhibit a significant amount of water content. The degradation behavior of the DTS samples, both with and without crosslinking, was evaluated in phosphate-buffered saline (PBS) to assess scaffold stability (Fig. 2M). After 7 days, DTS(ncr) without crosslinking exhibited a rapid degradation rate, leading to complete degradation, while the crosslinked DTS (cr) scaffold showed a degradation rate of 39.39 ± 0.55 %. At 28 days of incubation, the degradation rate of DTS(ncr) reached 85.72 ± 0.32 %. These findings indicate that the initial crosslinking of the bioink, along with the final crosslinking of the scaffold, contributed to a controlled degradation rate. Moreover, similar *in vivo* degradation behavior was observed in our previous study, where all samples were completely degraded within 2 months post-implantation [36].

The dual-release kinetics of FGF-18 and TGF-β1 from the 3D scaffolds were monitored over 21 days. Several studies have demonstrated that FGF-18 promotes chondrocyte migration, and proliferation and significantly induces ECM production to facilitate cartilage regeneration [73,74]. Furthermore, TGF-β1 acts as a pivotal regulatory factor that drives the progression of chondrogenic differentiation, and pre-chondrocyte proliferation, and ultimately inhibits terminal differentiation [75]. As

the stem cell undergoes a differentiation stage, the stem cell proliferation decreases notably. Additionally, the proteomics results also indicated that the proteins present in dECM could down-regulate cell proliferation and differentiation. Consequently, the synergistic effect of FGF-18 and TGF-β1 is very crucial in this study. Also, the combined influence of FGF-18, TGF-β1, and key components of dECM can activate the stem cell-migration process. The results depicted in (Fig. 2N) showed that more than 70 % of FGF-18 was released from the DTSTF scaffold after 7 days, while Fig. 2O revealed that 62 % of TGF-β1 was released from the DTSTF. After 21 days, the release profile demonstrated that 87 % and 71.5 % of FGF-18 and TGF-β1 had been released respectively. These results depicted the cumulative release profile, where TGF-β1 could stimulate chondrogenesis and FGF-18 could simultaneously enhance cell migration, proliferation, and ECM production and prevent the possible formation of calcified cartilage [76,77]. Therefore, this combination of dual-release and synergistic effects was further investigated for an *in vitro* cellular study.

2.3. *In vitro* biocompatibility, and chondrogenesis by synergizing effects of FGF-18 and TGF-β1 from the proteinaceous bioactive scaffolds

Adipose-derived stem cells (ADSCs) isolated from New Zealand white rabbits were cultured in this study to utilize with 3D bio-printing scaffolds and for *in vitro* studies (Fig. 3A). To confirm the synergizing effects of FGF-18 and TGF-β1 from the scaffolds, an *in vitro* wound healing assay and transwell cell migration assay were performed in this study. The results of the wound healing scratch assay presented in Fig. S8A demonstrated that DTSF and DTSTF significantly promoted cell migration toward the wound scratch area after 24 h of incubation. Furthermore, the results in Fig. S8B indicated that at 0 h, the width of the scratch area of all samples was approximately 15.65 %. After 24 h of incubation, the scratch closing gap percentage significantly decreased in both DTSF and DTSTF and 2.35 % and 1.03 % remained yet to be healed respectively. Additionally, a transwell-based cell migration assay was performed and the migrated cells were stained with crystal violet (Fig. 3B). A considerably higher number of migrated cells was observed for DTSTF, while DTST and DTSF showed an almost similar number of migrated cells. Therefore, statistical analysis results revealed the number of migrated cells per field was 168, 259, 321, and 592 for DTS, DTST, DTSF, and DTSTF respectively. DTSTF showed the highest number of migrated cells compared with the control and other samples (Fig. 3C). The wound healing and transwell migration assay confirmed that the cumulative release of FGF-18 from the scaffolds promotes cell proliferation and cell migration. Some studies have proved that the activation of the PI3K/AKT signaling pathway by FGF-18 regulates the cellular process of stem cells such as protein synthesis, migration, proliferation, cell survival, and glucose hemostasis [78–80]. Moreover, the ADSCs cannot migrate or proliferate in F12 media without serum. Therefore, the results of DTS and DTSF indicated that the key biological proteins in dECM stimulate the ADSCs migration process and direct the FGF-18 to promote cell proliferation and migration by activating the PI3K/AKT signaling pathway. Furthermore, the DTSTF scaffold showed the synergizing effects of FGF-18 and TGF-β1 on the ADSCs. Therefore, the dual-controlled release of FGF-18 and TGF-β1 and the proteins from the bioactive scaffold exceptionally increased the cell migration, and cell proliferation process.

The *in vitro* biocompatibility and cell viability of the 3D bio-printed scaffolds were confirmed by performing live/dead cell assay and MTT cytotoxicity assay. Some studies showed that the cell viability of the 3D bio-printed constructs is low due to the long printing duration and the high stress imposed on the cells during bio-printing [81–83]. In this study, after 7 days *of in vitro* culture, the live/dead cell assay fluorescence staining was conducted on ADSCs-loaded 3D scaffolds. The visual assay results (Fig. 3D) showed that DTST, DTSF, and DTSTF showed high cell viability compared to DTS. Additionally, the SEM observation revealed healthy cellular morphology. The results in Fig. 3F indicated that the cell viability of DTS, DTST, DTSF, and DTSTF were 74.23 ± 23.2 %, 80.17 ± 45.2 %, 83.79 ± 53.62 %, and 87.25 ± 12.2 % respectively. The MTT cytotoxicity assay resembles the live/dead cell viability assay. Fig. 3E demonstrates that DTSTF exhibited the highest absorbance value relative to DTS. These findings affirm that the synergizing release of FGF-18 and TGF-β1 significantly enhances cell viability and cell proliferation within the scaffold following 3D bio-printing.

Furthermore, it has already been proved that TGF-β1 is one of the key regulatory factors that control chondrogenesis [84–86]. The FGF-18 stimulates chondrogenesis for cartilage repair and in conjunction with other factors, exerts a synergistic effect on the chondrogenesis of Stem Cells [74,87]. Therefore, in this study, we observed the chondrogenesis of rabbit-derived ADSCs through the synergistic effect of FGF-18 and TGF-β1 along with key biological proteins associated with chondrocyte differentiation in dECM-loaded proteinaceous bioactive scaffold extract media. In this study, ADSCs pellets were cultured for 21 days in an extraction media that contained FGF-18 and TGF-β1 growth factors. The cell pellets (Fig. 3G) were further proceeded for histological and immunofluorescence staining to confirm the chondrocyte differentiation after 21 days of incubation. Fig. 3H showed that the pellet volume after 21 days of culture was found 6.2 ± 12.5 mm^3, 13.6 ± 10.2 mm^3, 18.17 ± 45.7 mm^3, and 15.08 ± 32.6 mm^3 for DTS, DTST, DTSF, and DTSTF respectively. Due to the release of FGF-18 cell proliferation, ECM deposition was exceeded, thus the pellet volume of DTSF was also increased. However, the pellet volume of DTSTF remained well controlled and formed a perfectly round shape due to the controlled release of the dual growth factors. During chondrogenesis, the ADSCs differentiated into mature chondrocytes, and finally, the terminal differentiation occurred by differentiating into hypertrophic chondrocytes (Fig. S9A). In Figure S9B, H&E staining demonstrated that in the DTST and DTSTF groups, the ADSCs morphology was completely differentiated to chondrocytes compared to the control. Nonetheless, most of the cells in the DTSF group remained at the chondrocyte-differentiating stage. The histological staining results (Fig. 3I) with Safranin-O/Fast green and Alcian blue/Nuclear fast red revealed that more intense staining of red and blue color was observed in the DTST and DTSTF groups. The results indicated that a high amount of proteoglycan and glycosaminoglycan (sGAG) was formed in the DTST and DTSTF groups compared to DTS and DTSF. All the results strongly confirmed that the synergistic effect of FGF-18 and TGF-β1 along with key biological proteins from the proteinaceous bioactive scaffolds stimulates chondrocyte differentiation. Therefore, we predict that the key biological proteins of the bioactive scaffold direct both FGF-18 and TGF-β1 to activate the PI3K/AKT and TGF-β1-Smad4 signaling pathways and that potentially increase the ECM production, total amount of collagen, and sGAG content, and ultimately inducing the chondrogenic differentiation [79,88,89]. To validate this, chondrogenesis was further confirmed by immunofluorescence staining using key relevant proteins Col2, ACAN, and PRG4 (Fig. 3J) and evaluated the expression of cartilage-related genes by Reverse transcription-polymerase chain reaction (RT-PCR). The results indicated that all chondrogenic markers were highly expressed in the groups of DTST and DTSTF. The semi-quantitative analysis results in Fig. 3K, L, and M further indicated that the intensity of Col2, ACAN, and PRG4 were firmly expressed in both DTST and DTSTF groups and suggesting that DTSTF has more suitable microenvironment for chondrogenic differentiation than other groups. The RT-PCR results in Fig. S9C show that the expression of chondrogenic gene (Sox9) in the DTSTF was elevated by 3.36 fold compared to the negative control group, which revealed the ability of DTSTF to promote chondrogenic differentiation of ADSCs and potentially restrain hypertrophy. Additionally, we analyzed the total collagen and sGAG concentration of the samples. The results (Fig. 3N) of the total collagen concentration of DTST, DTSF, and DTSTF were 46.52 μg/mg, 36.23 μg/mg, and 52.18 μg/mg respectively. Moreover, the total sGAG concentrations (Fig. 3O) were 0.15 μg/mg, 0.13 μg/mg, and 0.16 μg/mg of DTST, DTSF, and DTSTF respectively. In all groups, the total collagen and sGAG levels significantly increased

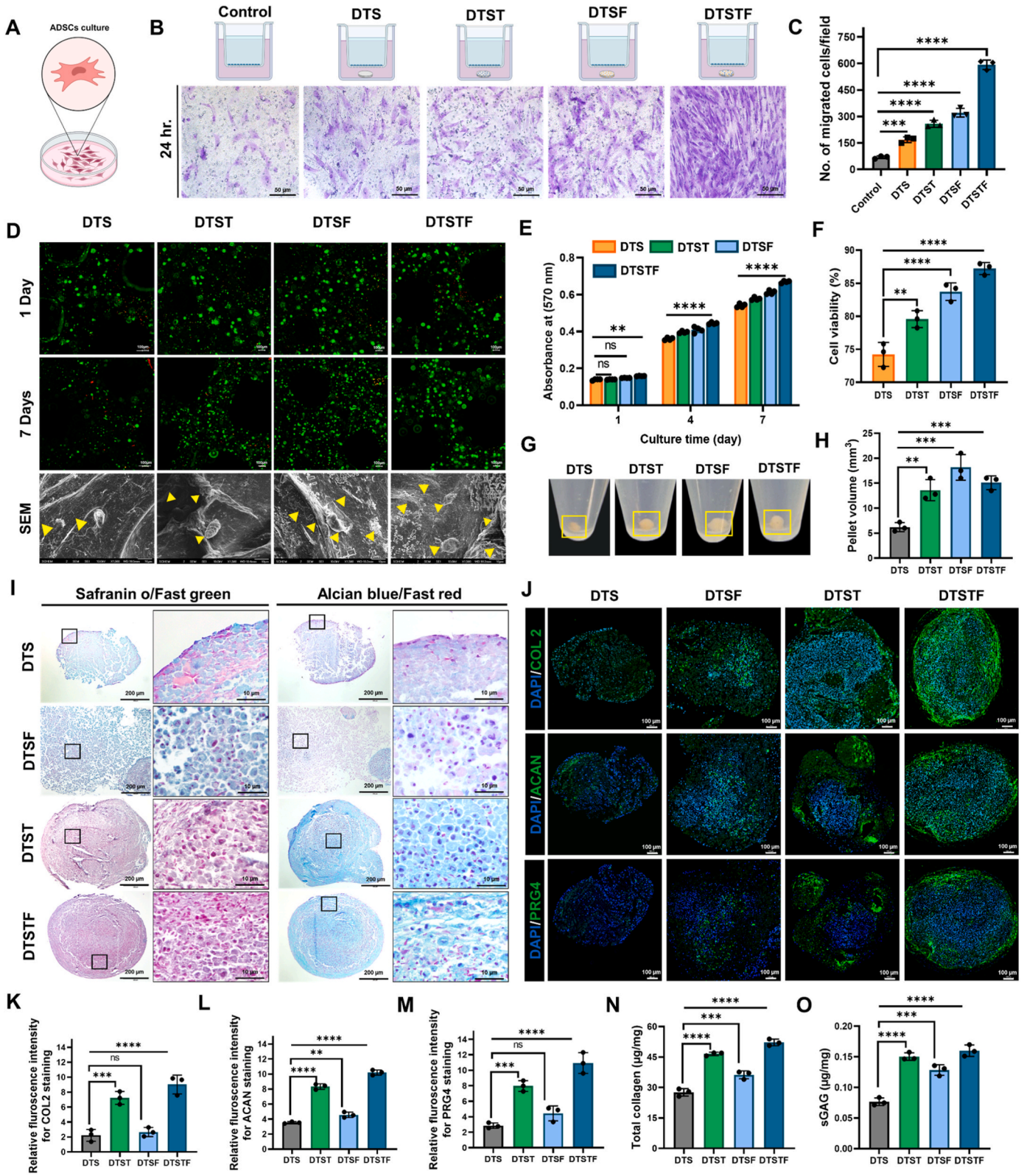

Fig. 3. *In vitro* biocompatibility and chondrogenic differentiation by synergistic effects of FGF-18 and TGF-β1 from the proteinaceous bioactive scaffold. (A) *In vitro* culture of adipose-derived stem cells (ADSCs). (B) Transwell-based cell migration assay of different sample groups. Scale bar: 50 μm (C) Quantification of migrated cells after 24 h. (D) Live/dead cell assay and SEM analysis for cell distribution morphology after 7 days of culture. Scale bar: 100 μm (E) MTT cytotoxicity analysis after 1, 4, and 7 days. (F) Quantification of cell viability analysis after 24 h. (G) Optical image of the ADSCs cell pellets after 21 days of chondrogenic differentiation. (H) Quantification of pellet volume analysis (I) Histological analysis for chondrogenesis of the ADSCs cell pellets. Safranin-O and Alcian blue staining after 21 days of implantation. Scale bar: 200 μm, 10 μm. (J) Immunofluorescence staining of chondrogenesis marker COL2, ACAN, and PRG4. Scale bar: 100 μm. Quantitative analysis of (K) COL2, (L) ACAN, and (M) PRG4 positive staining after 21 days of differentiation. (N) Total collagen and (O) sGAG quantification. Data are presented as mean ± SD.

compared to the control. These results suggest that the therapeutic effects of DTSTF on ADSCs predominantly rely on the activation of the PI3K/AKT and TGFβ1/Smad4 signaling pathways, coupled with the synergistic effect of FGF-18 and TGF-β1.

2.4. Evaluation of in vivo cartilage tissue regeneration and in silico docking simulation

The *in vivo* investigation was performed in 6 months-old New Zealand white rabbit model and after implantation of 3D scaffolds at the defect site, the animals were monitored for 3 and 6 months. These time

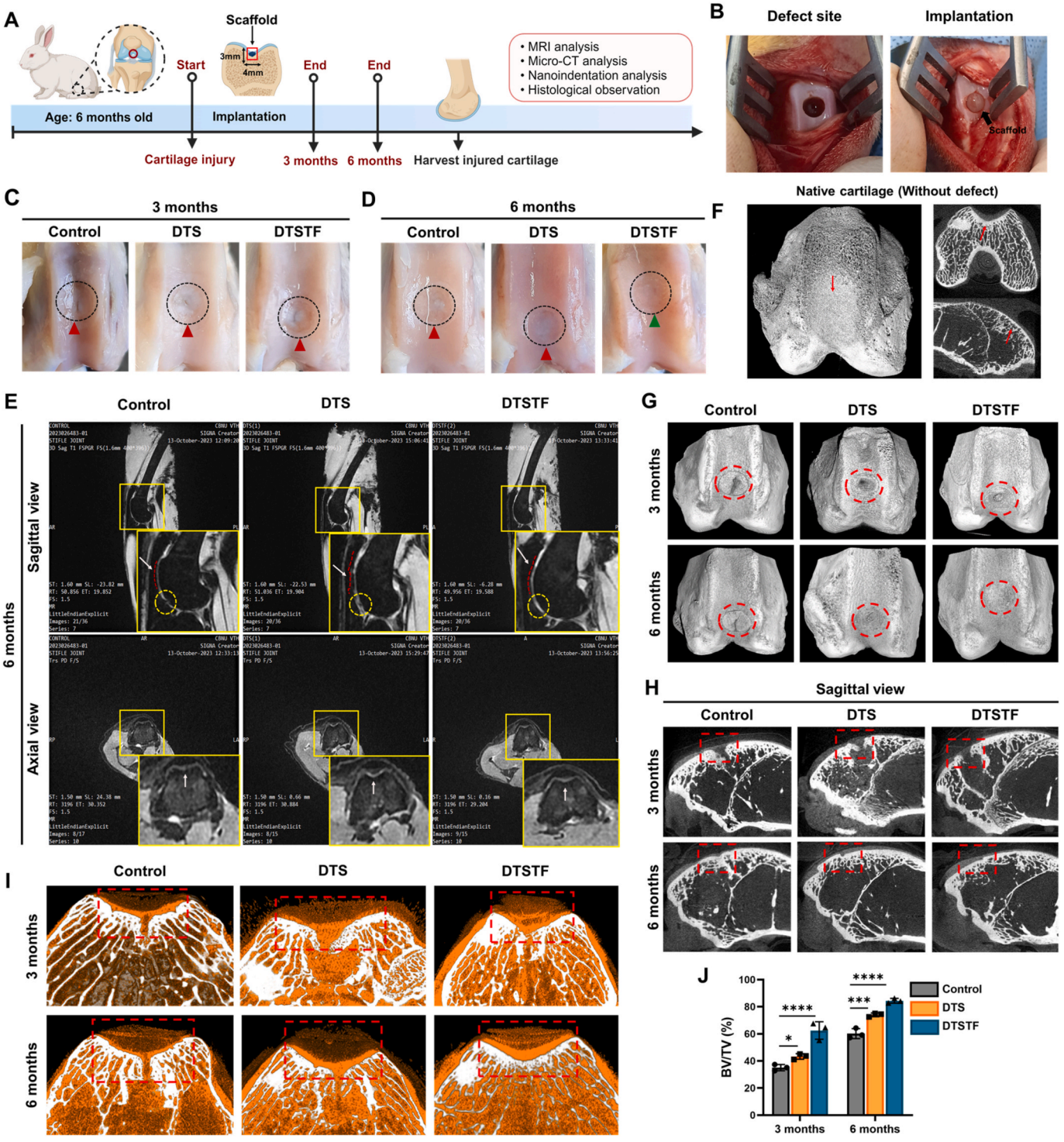

Fig. 4. (A) Schematic illustration of a rabbit injury model, implantation, and investigation procedures. (B) Optical images of the rabbit knees cartilage defect model and 3D bio-printed scaffold implantation. (C) *In vivo* samples after 3 months of post-surgery and (D) 6 months of post-surgery. (E) MRI analysis after 6 months. Red dotted line shows the shape of the native cartilage structure after 6 months (F) Micro-CT analysis of native cartilage sample. Micro-CT analysis of (G) Top view (H) Sagittal view of the regenerated cartilage samples after 3 months and 6 months. (I) 3D M-CT analysis of the cartilage samples (J) Quantification of bone volume/tissue volume fraction. Black, yellow and red dotted circle and red dotted rectangular indicating the defect site. Data are presented as mean ± SD.

frames allowed for the proper evaluation of cartilage healing, which is a slow process due to the avascular nature of the tissue. Monitoring over an extended period was essential to assess long-term regeneration outcomes. Additionally, this approach aligns with current research, allowing for meaningful comparisons with other research studies [90–94]. The total experimental outline is illustrated in Fig. 4A. Moreover, Fig. 4B depicts a cartilage defect measuring 3 mm × 4 mm and the implantation of a 3D bio-printed scaffold designed to mimic the size and shape of the cartilage defect. Three groups were divided to conduct the investigation: Control (without treatment), DTS, and DTSTF. After 3 months post-surgery, the results (Fig. 4C) indicated that the cartilage defects in the control and DTS groups had not healed, while the DTSTF group showed slight healing. However, results after 6 months post-surgery (Fig. 4D) revealed that defects in the Control group remained unfilled, the DTS groups were healed but the surface of regenerated cartilage was uneven. By contrast, the cartilage defects in the DTSTF groups were

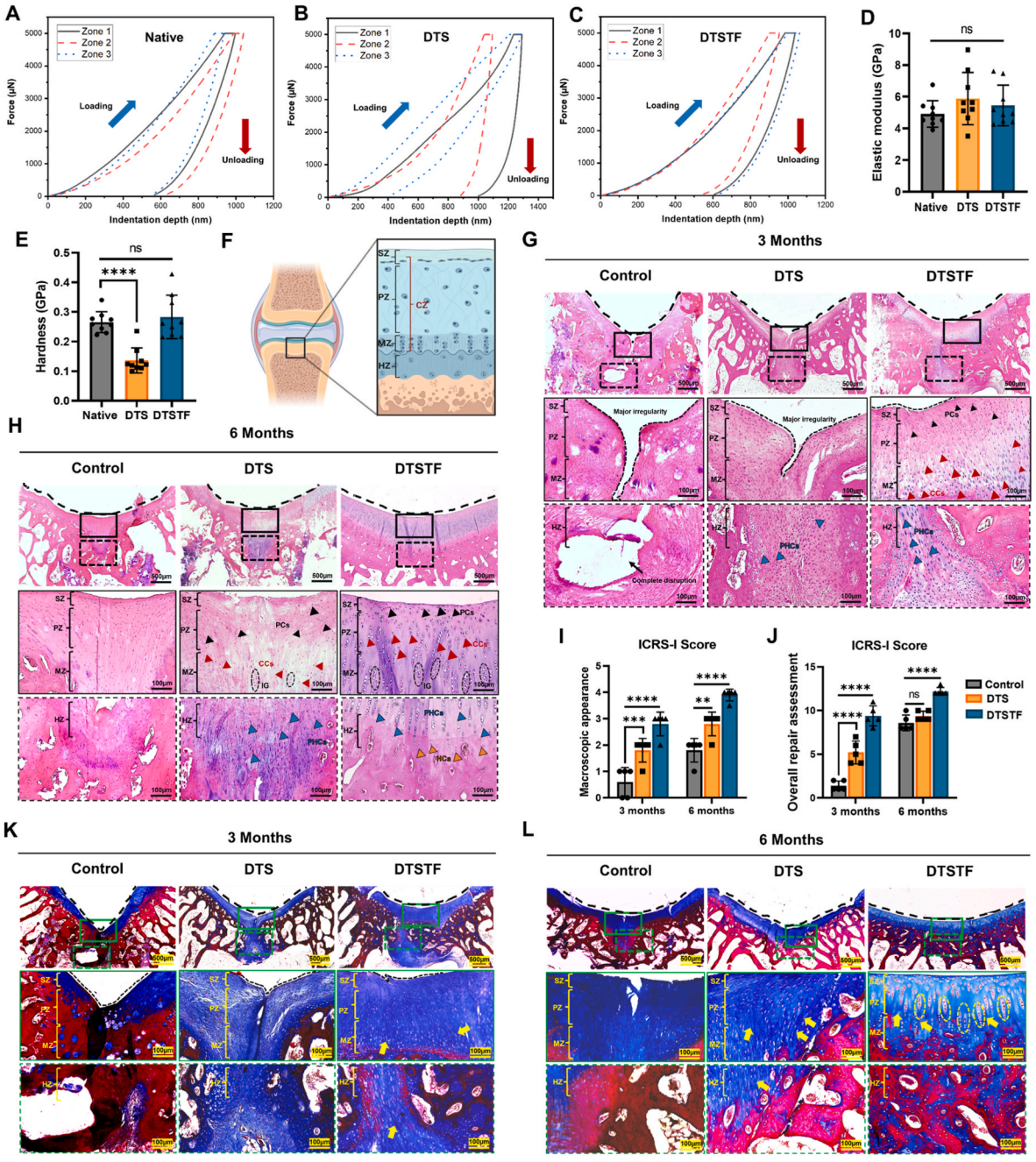

Fig. 5. *In vivo* biomechanical analysis of regenerated cartilage samples after 6 months of post-surgery by nanoindentation technique. The force vs indentation depth curves for *in vivo* samples of (A) Native, (B) DTS, and (C) DTSTF. (D) Elastic modulus and (E) Hardness of the regenerated cartilage samples. (F) A schematic illustration of different zones of the cartilage layer with chondrocyte morphology. Histological analysis for chondrocyte morphology in different zonal areas of regenerated cartilage. H&E and Masson's trichrome staining of the samples after (G, K) 3 and (H, L) 6 months of implantation. Scale bar: 500 μm and 100 μm. The black dotted line represents the surface of the regenerated cartilage. (I, J) Articular Cartilage Repair Assessment analysis by the International Cartilage Repair Society-I (ICRS-I) scoring system. The black arrowhead: PCs, the Red arrowhead: CCs, the Blue arrowhead: PHCs, and the Orange arrowhead: HCs. The black line box indicated the interface of the defect site, and the dotted box indicated the inner side of the cartilage. The black dotted circles are IG. SZ: Superficial Zone, PZ: Proliferating Zone, MZ: Maturation Zone, CZ: Chondrocyte Zone, HZ: Hypertrophic Zone, PCs: Proliferating Zhondrocytes, CCs: Condylar Chondrocytes., PHCs: Pre-Hypertrophic Chondrocytes, IG: Isogenic Group, HCs: Hypertrophic Chondrocytes. Data are shown as mean ± SD.

successfully repaired with full thickness of cartilage tissue. Notably, the regenerated cartilage of the DTSTF groups was more mature and mechanically dense than that of the DTS group. Additionally, to confirm cartilage regeneration at the defect site and to examine the surface morphology of the whole knee joint MRI was performed on the 6-month samples (Fig. 4E). The results of the control group in both sagittal and axial view showed that the defect site (indicated by a dotted yellow circle) was not healed. In the DTS group, the cartilage defect healed slightly though the thickness of the regenerated cartilage was thinner than the native cartilage, and the OA was observed on the upper side of the knee joint. In contrast, the DTSTF group cartilage defect was well integrated and regenerated with dense, thick cartilage, and the surface of the regenerated cartilage was smooth and closely mimicked that of the native cartilage. Furthermore, micro-CT analysis was performed to assess the new subchondral bone formation. Fig. 4F and G shows that the defect region in the DTSTF group was filled with dense subchondral bone that was well integrated with the native subchondral bone tissue after 6 months of implantation. Notably, relatively poor bone regeneration was observed in the DTS group. Moreover, the center of the defect region surface in the DTS group was notably thinner and more irregular compared to the native and the control group still had an obvious crack at the center of the defect site. Fig. 4H and S10A displayed the sagittal and axial views of the implantation region, highlighting the surface of the subchondral bone in the DTS group has a rough and irregular surface morphology and the regenerated area was very thin. In contrast, the DTSTF group found a regular and smooth subchondral bone formation after 6 months. Furthermore, 3D image analysis of micro-ct was conducted to closely observe the defect site and the newly regenerated subchondral bone and soft tissue (Fig. 4I). The analysis revealed the new subchondral bone formation in white and the new soft tissue regeneration in orange. The 3D clearly showed that the DTSTF group displayed a very smooth and regular subchondral surface, with a formation of a thick layer of cartilage tissue compared to the control and DTS groups.

Furthermore, the data analysis (Fig. 4J) indicated that, compared with the control and DTS groups, the bone-volume fraction (BV/TV) was significantly enhanced in the DTSTF group after 3 and 6 months. The results revealed the BV/TV percentage for control, DTS, and DTSTF at 35.09 ± 45.2 %, 43.35 ± 23.1 %, and 62.49 ± 12.8 % after 3 months respectively. The ratio markedly increased after 6 months of implantation and showed the percentages of control, DTS, and DTSTF of 60.20 ± 10.01 %, 74.06 ± 15.32 %, and 84.40 ± 21.2 % respectively.

Dynamic nanoindentation testing was conducted on the regenerated cartilage to evaluate the biomechanical properties, including elastic modulus, and hardness of the cartilage. To perform the analysis, 3 zones were identified at the center of the defect region (Fig. S10B). Fig. 5A, B, and C represent the force-depth relationship of the native and regenerated cartilage of DTS and DTSTF groups. The results revealed that at 5000 μN, the indentation depths of the native cartilage from 3 zones were almost similar approximately around 600 nm, and the DTSTF group undoubtedly closely mimicked the native cartilage. These findings confirm that the surface of the DTSTF cartilage was smooth and very regular similar to a healthy native cartilage. Nevertheless, the force-depth curves of the DTS group's 3 zones did not align. The data showed the indentation depths of Zone 1, Zone 2, and Zone 3 as 1028.2 ± 63.2 nm, 879.9 ± 40.4 nm, and 411.14 ± 23.5 nm respectively, indicating a rough and irregular surface and the cartilage mechanical properties were not similar. Zone 3 exhibited significantly softer cartilage compared to Zone 1. Furthermore, the elastic modulus results (Fig. 5D) demonstrated that the DTSTF had a very similar elastic modulus compared to that of the native cartilage. The results showed the elastic modulus of native, DTS, and DTSTF at 4.91 ± 58.3 GPa, 5.88 ± 41.2 GPa, and 5.42 ± 25.41 GPa respectively. These results indicated the excellent flexibility and deformability of the DTSTF group resembles the native cartilage. Moreover, the hardness of the DTSTF (Fig. 5E) indicated that the regenerated cartilage exhibited high resistance to deformation under an applied force compared to the DTS. Finally, the comprehensive biomechanical results of the nanoindentation clearly demonstrated that the DTSTF formed a mechanically dense and robust cartilage tissue, highly comparable to native cartilage.

Cartilage, a thin connective tissue, is composed of four layers: the superficial zone, proliferating zone, maturation zone, and hypertrophic zone. Among the layers, the main chondrocyte zone consists of the superficial to maturation zone (Fig. 5F). In each layer, the chondrocyte morphology is also different according to the differentiation stage. In this study, the *in vitro* results already confirmed that the ADSCs-laden DTSTF scaffold has the potential to differentiate the stem cells into chondrocytes. Therefore, the *in vivo* histological analysis was conducted after 3 and 6 months of implantation to confirm the chondrocyte differentiation and analyze the cell morphology and cartilage regeneration, where the black box indicates the interface of the defect site and the black dotted box indicates the inner zone of the defect site. The H&E staining results (Fig. 5G) revealed that after 3 months of implantation, the defect had not properly regenerated in the control and DTS group. In the case of control, the superficial zone showed a major irregular surface, and a large void was observed on the inner side of the hypertrophic zone. Moreover, the DTS group displayed also a major irregular surface in the superficial zone and the hypertrophic zone observed pre-hypertrophic chondrocytes (PHCs) which were marked with the blue arrowhead. We hypothesized that the key biological proteins from the proteinaceous bioactive scaffold facilitate the cell migration process from the subchondral layer, influencing cell differentiation according to the morphological characteristics of the hypertrophic zone.

The DTSTF group demonstrated complete repair of the cartilage defect, although the surface of the superficial zone was irregular and not smooth. Moreover, a substantial number of proliferating chondrocytes (PCs) were observed in the superficial zone (black arrowhead), while condylar chondrocytes (CCs) appeared in the proliferating zone, and maturation zone (red arrowhead), and PHCs were noted in the hypertrophic zone (blue arrowhead). However, no mature chondrocytes or isogenic groups of chondrocytes were observed in the maturation zone. The ADSCs began to proliferate, migrate, and differentiate from the superficial zone to the hypertrophic zone. Simultaneously, the cell migration process was also activated from the subchondral zone, evident in the hypertrophic zone of the cartilage. After 6 months of implantation, the results (Fig. 5H) indicated that both the control and DTS groups still presented a rough cartilage surface on the superficial layer. There were no differentiated chondrocytes were observed in the control group. The DTS group observed very few PCs, CCs, and PHCs in the chondrocyte zone to the hypertrophic zone. Some isogenic groups of chondrocytes were also observed in the maturation zone of the DTS. Finally, the DTSTF group observed the complete regeneration of the full thickness of cartilage tissue. The surface of the superficial zone was also smooth and found regularly shaped. The scaffold was completely degraded after 3 months of implantation. A significant presence and proper distribution of PCs, CCs, PHCs, and hypertrophic chondrocytes (HCs) were observed from the superficial zone to the hypertrophic zone. Numerous isogenic groups of chondrocytes were identified within the maturation zone, while no hypertrophic chondrocytes were found from the superficial to maturation zones. This distribution of chondrocytes indicates that the synergistic effect of the dual growth factors effectively accelerates chondrogenic differentiation while delaying terminal hypertrophic differentiation, allowing ADSCs to differentiate appropriately according to each specific cartilage zonal area. Moreover, there was no vascular infiltration and ossification was observed during the regeneration process after 3 and 6 months of implantation on the defect site. Furthermore, the Articular Cartilage Repair Assessment was analyzed by the International Cartilage Repair Society-I (ICRS-I) scoring system (Table S6). The scoring was analyzed by individual observers based on the regenerated cartilage surface, and regeneration area. The results of both microscopic appearance (Fig. 5I) and overall repair assessment (Fig. 5J) scoring indicated that DTSTF has better cartilage regeneration compared to the control and DTS groups. Additionally,

Mason's trichrome staining results (Fig. 5K and L) confirmed high expression of total collagen, evidenced by the intense blue staining of the regenerated cartilage after 3 and 6 months. The results observed that a significant amount of fibrous collagen tissue was formed in both the DTS and DTSTF groups after 6 months. Therefore, these findings deliberately proved the synergistic effect of FGF-18, TGF-β1, and the proteins released from the proteinaceous bioactive DTSTF scaffold, which enhanced the cell recruitment, proliferation, migration, differentiation, and finally regenerated cartilage damage.

In addition, the histological analysis of Safranin-o/fast green staining (Fig. 6A and B) and Alcian blue/nuclear fast red staining (Fig. 6C and D) were conducted to further evaluate the chondrogenesis and cartilage regeneration. The safranin-o was used to observe the formation of proteoglycan amount in the regenerated cartilage matrix which was expressed as a dark red color. Results after 3 months of implantation indicated that proteoglycan formation was less prominent in the control and DTS groups compared to the DTSTF group. Due to the synergistic release of FGF-18 and TGFβ-1 from the DTSTF scaffold, the ECM deposition was increased and the stem cell migration effect was induced. Therefore, the proteoglycan formation was significantly increased in the inner layer of the hypertrophic zone. After 6 months of implantation, the DTSTF group expressed a significant amount of proteoglycan by forming a dark red intense staining color. The chondrocyte differentiation, matrix production, and cell migration were achieved successfully and

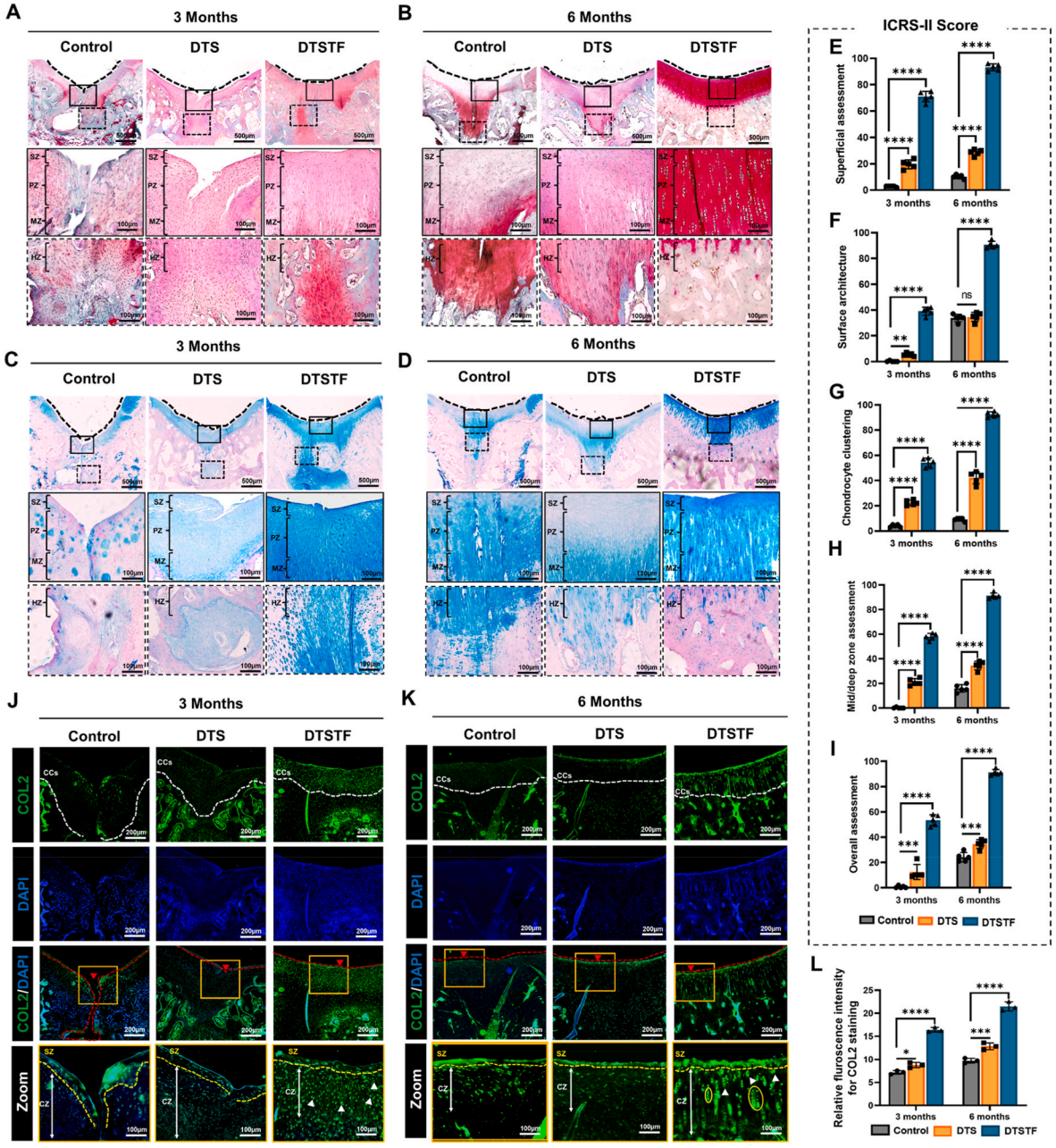

Fig. 6. *In vivo* histological analysis for chondrogenesis and cartilage regeneration. Safranin-o/fast green staining for proteoglycan formation after (A) 3 and (B) 6 months of implantation. Alcian blue/nuclear fast red staining for sGAG formation after (C) 3 and (D) 6 months of implantation. Scale bar: 500 μm and 100 μm. (E–I) The International Cartilage Repair Society II (ICRS-II) histological scoring system for cartilage regeneration. Immunofluorescence staining of cartilage-specific marker COL2 expression profile after (J) 3 and (K) 6 months of post-surgery. Scale bar: 200 μm and 100 μm. (L) Quantitative analysis of COL2 positive staining area after 3 and 6 months. White dotted line: Condylar chondrocytes zone. The red line with the arrowhead represents the cartilage surface with the defect site. Yellow dotted line: Superficial zone. White arrowhead: Chondrocytes. Yellow circle: Isogenic groups. Data are presented as mean ± SD.

uniformly distributed in the DTSTF group. In contrast, the control and DTS groups observed less amount of the expression of proteoglycan formation. Similarly, the Alcian blue staining results (Fig. 6C and D) also resemble the safranin-o staining results. The DTSTF group demonstrated superior outcomes in terms of sGAG expression, matrix staining, and cartilage integrity. Histological analysis, as reflected in the ICRS-II histological scoring system (Table S7) in Fig. 6E, F, G, H, and I represents superficial assessment, surface architecture, chondrocyte clustering, mid/deep zone assessment, and overall assessment indicates that the proteinaceous bioactive DTSTF scaffold after 3 and 6 months exerts the highest score, suggesting a significant therapeutic effect in chondrogenesis and repairing cartilage damage.

To explore the *in vivo* synergistic effect of FGF-18 and TGF-β1 derived from the proteinaceous bioactive scaffold DTSTF, key proteins related to the cartilage ECM were analyzed via immunofluorescence staining. As depicted in Fig. 6J, after 3 months of implantation COL2 expression was highly expressed in the DTSTF group compared to the control and DTS groups. Notably, this expression was predominantly enhanced in the central zone of the cartilage defect which was marked with a red arrowhead. Further, in Fig. 6K, the results after 6 months of implantation showed that both DTS and DTSTF expressed a significant expression of COL2 marker, indicating the key biological proteins present within the dECM, along with FGF-18 and TGF-β1 modulate the key essential factors of the PI3K/AKT and TGFβ1/Smad4 signaling pathways. Both FGF-18 and TGF-β1 were found to regulate the function of COL2 up-regulation, and synergistically promoted chondrocyte proliferation and migration. The fluorescence intensity results (Fig. 6L) indicated the pronounced expression profile of COL2 from the DTSTF scaffold.

Furthermore, immunofluorescence staining was performed using the superficial zone chondrocyte markers of Aggrecan (ACAN) and Proteoglycan 4 (PRG4). These markers are also key regulatory proteins in the PI3K/AKT and TGFβ1/Smad4 signaling pathways. The results of ACAN staining depicted in Fig. 7A and B indicated a high expression profile in the superficial zone of the DTSTF group after 3 and 6 months of implantation, where the superficial zone was indicated with the yellow color dotted line in the zoom image. Additionally, the chondrocytes and isogenic groups were observed in the chondrocyte zone of DTSTF. In contrast, the expression profile of control and DTS were significantly poorer when compared to DTSTF. Fig. 7E shows that relative

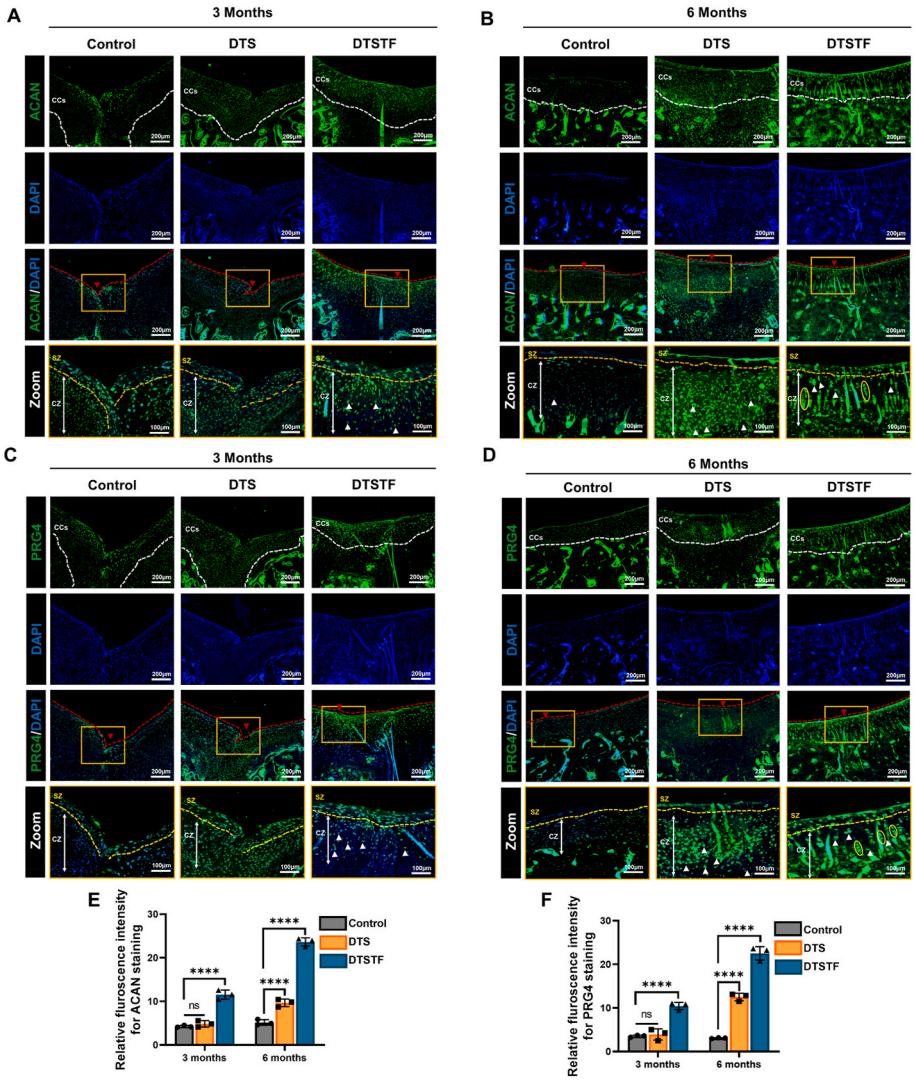

Fig. 7. Immunofluorescence investigation for the *in vivo* synergistic effect of FGF-18 and TGF-β1. (A, B) Expression profile of cartilage-specific marker Aggrecan (ACAN) after 3 and 6 months of post-surgery. (C, D) Expression profile of cartilage superficial zone markers Proteoglycan 4 (PRG4) after 3 and 6 months of post-surgery. (E). Quantitative analysis of ACAN positive staining area after 3 and 6 months. (F) Quantitative analysis of PRG4 positive staining area after 3 and 6 months. Scale bar: 200 μm and 100 μm. White dotted line: Condylar chondrocytes zone. The red line with the arrowhead represents the cartilage surface at the defect site. Yellow dotted line: Superficial zone. White arrowhead: Chondrocytes. Yellow circle: Isogenic groups. Data are shown as mean ± SD.

fluorescence intensity results also confirmed that after 6 months of implantation, ACAN was highly expressed in the DTSTF group. Moreover, results from PRG4 staining (Fig. 7C and D) demonstrated that the DTSTF group exhibited a high expression profile after 3 and 6 months. Conversely, the control and DTS group's expression profiles were down-regulated due to the absence of FGF-18 and TGF-β1. In Fig. 7F, the relative fluorescence intensity results confirmed the up-regulation of PRG4 expression in the DTSTF scaffold after 3 and 6 months of implantation.

All the evaluation results directly indicated that the synergistic effect of FGF-18 and TGF-β1 activates the PI3K/AKT and TGFβ1/Smad4 signaling pathways, which in turn actively regulates the ADSCs proliferation, migration, chondrocyte differentiation, and finally cartilage regeneration by proteinaceous bioactive scaffold. Consequently, the computational protein-protein docking simulation study and immunofluorescence staining with Smad4 and AKT were conducted to demonstrate the binding affinity and elucidate the mechanism of PI3K/AKT and TGFβ1/Smad4 molecular signaling pathways in inducing chondrogenesis and cartilage regeneration. The involvement of TGF-β1 is notably diverse, it participates in several biological processes [95]. However, the early-stage chondrogenesis effect initiates when TGF-β1 actively interacts with the TGFβ type II receptor. Accordingly, we examined the binding affinity between TGF-β1 and TGFβ-RII receptors. In Fig. 8A, it was observed that among the several interactions, chain D of TGF-β1 and chain A of TGFβ-R2 exhibited the highest binding affinity. A total of 29 receptors on chain A interact with the 25 receptors on chain D (Fig. 8B), where the binding interaction was attained by 1 salt bridge, 7 hydrogen bonds, and 140 non-bonded contact interactions between the two molecules. These receptor bindings between chain A and chain D are represented in Fig. 8C. Moreover, the high expression profile of Smad4 in the DTSTF scaffold, as shown in Fig. 8D, demonstrates the activation of the TGFβ1/Smad4 signaling pathway at 6 months

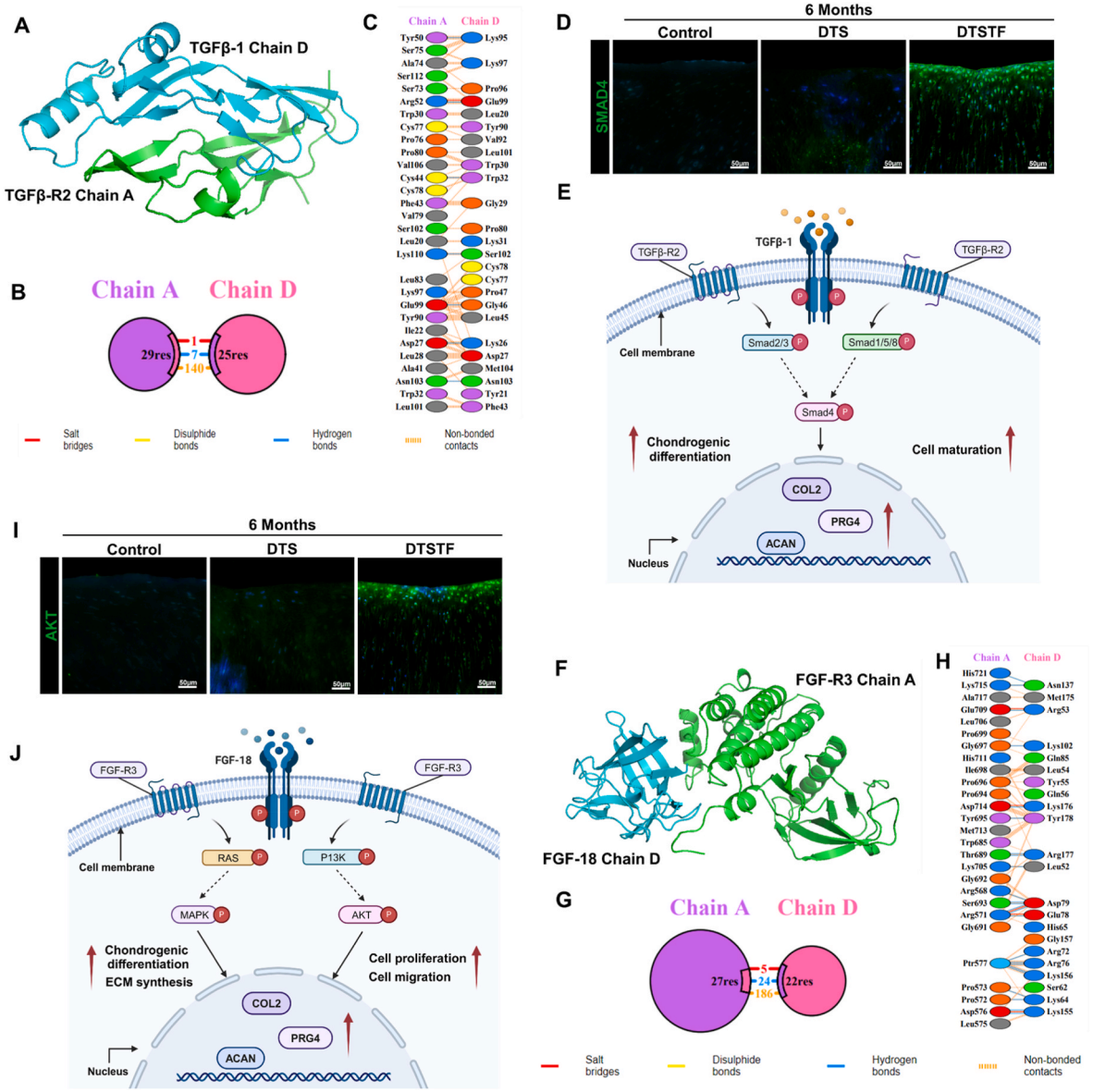

Fig. 8. In silico docking analysis of the synergistic effect of FGF-18 and TGF-β1 in activating the TGFβ1/Smad4 and PI3K/AKT signaling pathways. (A) Possible binding sites between the TGF-β1 chain D and the TGFβ-RII chain A. (B, C) Number of receptor bindings and their interactions between chain D and chain A. (D) Expression profile of Smad4 for the confirmation of TGFβ1/Smad4 signaling pathway. Scale bar: 50 μm (E) Schematic illustration of the TGF-β1 activating TGFβ1/Smad4 signaling pathway. (F) Possible binding sites between the FGF-18 chain D and the FGF-R3 chain A. (G, H) Number of receptor bindings and their interactions between chain D and chain A. (I) Expression profile of AKT for the confirmation of PI3K/AKT signaling pathway. Scale bar: 50 μm (J) Schematic illustration of the FGF-18 activating PI3K/AKT signaling pathway.

post-implantation, in contrast to the control and DTS groups. The primary mechanism of the TGF-β1 signaling pathway for chondrogenesis begins when the TGF-β1 chain D binds with the TGFβ-RII chain A receptor, subsequently activating the type I receptor by the type II receptor, resulting in the phosphorylation of Smad2/3 and Smad1/5/8 signaling pathways. This signaling cascade further activates the downstream molecule Smad4, which is translocated into the nucleus (Fig. 8E) [60,96–99]. As a consequence, the expression of COL2, ACAN, and PRG4 is increased, thereby stimulating chondrogenic differentiation and cell maturation.

Furthermore, the FGF-18 could stimulate cell proliferation, cell migration, and ECM production. However, the effect of FGF-18 on chondrogenesis is still unknown [100,101]. Some studies showed that FGF-18 strongly binds with the FGF-R3 receptors and activates the downstream proteins. Therefore, the binding affinity between FGF-18 and FGF-R3 was examined, and observed that chain D of FGF-18 strongly binds with chain A of FGF-R3 (Fig. 8F). A total of 22 receptors of chain D interacts with the 27 receptors of chain A (Fig. 8G). Most of the binding interaction was attained by 5 salt bridges, 24 hydrogen bonds, and 186 non-bonded contact interactions between the two molecules. All the receptors binding between chain D and chain A are represented in Fig. 8H. Additionally, the high expression profile of AKT in the DTSTF scaffold, as illustrated in Fig. 8I, reveals activation of the PI3K/AKT signaling pathway, in comparison to the control and DTS groups. Some studies proved that FGF-18 upregulated FGF-R3 receptors [52,79]. Therefore, the mechanism of the PI3K/AKT signaling pathway for cell proliferation, migration, matrix production, and chondrogenesis started when FGF-18 chain D strongly binds with the FGF-R3 chain A receptor, subsequently, the tyrosin kinase of a domain of FGF-R3 chain A located inside the cell membrane was activated. This result further activates the downstream signals of RAS and MAPK pathways. On the other hand, it significantly activates the P13K and AKT at the same time. All those activated signals translocate into the nucleus and the expression profile of COL2, ACAN, and PRG4 was increased significantly (Fig. 8J) [52,60,79,102–104]. Therefore, the results demonstrated that activation of the PI3K/AKT and RAS-MAPK signaling pathways stimulates chondrogenesis. Furthermore, the binding energy between TGF-β1/TGFβ-R2 and FGF-18/FGF-R3 was found 897.18 ± 23.5 Δ G and 708.325 ± 42.9 Δ G respectively (Fig. S11). Finally, all the results significantly proved that 3D bio-printed proteinaceous bioactive scaffolds with the dual-release of TGF-β1 and FGF-18 promisingly increase ECM production, cell proliferation, cell migration, cell differentiation, and cartilage regeneration.

3. Conclusion

In summary, we introduced a novel FGF-18/TGF-β1 difunctional 3D bio-printed proteinaceous bioactive scaffold for cartilage tissue regeneration. The integration of natural porcine cancellous bone ECM, nanocellulose, and difunctional growth factors combined with stem cell-laden (ADSCs) advanced 3D bio-printing techniques, enhanced the scaffold's overall functionality. The unique design of biomaterials enabled the DTSTF scaffold to be applied directly to the surgical site by replicating the cartilage defect. Characterization results demonstrated that the scaffold was mechanically stable and facilitated a controlled release of TGF-β1 and FGF-18 from the bioactive scaffolds. Furthermore, the *in vitro* findings confirmed that the bioactive scaffold contained key biological proteins along with the synergistic effect of FGF-18 and TGF-β1 effectively maintained a favorable microenvironment for cell proliferation, cell migration, ECM synthesis, chondrogenic differentiation and notably, the activation of the TGFβ1/Smad4 and PI3K/AKT signaling pathways. Subsequently, both the *in vivo* studies and in silico docking simulations revealed that the DTSTF scaffold promoted matrix production, and the regeneration of mechanically robust, full-thickness cartilage tissue that closely resembles native cartilage in the defect region, bolstered by the dual effect of FGF-18 and TGF-β1. Overall, these findings suggest that this unique study concept of stem cell-laden proteinaceous bioactive scaffold could be a promising strategy to stimulate chondrogenesis and in situ cartilage regeneration.

4. Experimental section

4.1. Decellularization process of porcine cancellous bone

The decellularization process was followed by our previously published protocol [36]. Briefly, after receiving the cancellous bones, the bones were extensively washed with phosphate-buffered saline (PBS) to eliminate the residual tissue and immersed in liquid nitrogen to sectioned into small fragments. Subsequently, the fragments were processed through demineralization in 0.5 N HCl at room temperature for 24 h. Furthermore, post-demineralization, the fragments were washed in DW, and the lipid removal process was carried out using a 1:1 mixture of chloroform (Sigma-Aldrich, USA) and methanol (Sigma-Aldrich, USA) for 1 h and then repeatedly washed with methanol and distilled water. Then the bone fragments were lyophilized overnight. Finally, the lyophilized bone fragments were decellularized in 0.05 % trypsin and 0.02 % ethylenediamine tetraacetic acid (EDTA) (Sigma-Aldrich, USA) at 37 °C for 24h under continuous agitation. After the decellularization, the bones were washed with PBS supplemented with 1 % w/v penicillin/streptomycin for 24h at 4 °C and lyophilized again overnight. Finally, decellularized bones were crushed to obtain a fine bone powder with a cryogrinder (Retsch, mixer mill, MM 400) and stored at −80 °C until required.

The ECM digestion process was conducted with 1 mg/mL of pepsin (Sigma-Aldrich) in 0.01 N HCl solution, where the concentration of lyophilized bone powder was 10 mg/mL. The fine bone powder of dECM was stirred continuously until no visible particles of bone powder remained. The neutralization process involved mixing, 100 mL of a 10 mg/mL suspension, 50 mL of dECM suspension, 10 mL 10 × PBS, 2 mL 0.1 N NaOH, and 38 mL 1 × PBS were mixed and stored at −20 °C until required (Fig. 3A).

4.2. Characterization of decellularized ECM

To confirm the efficacious decellularization process, the detection of the remaining DNA quantity was initially observed. The Quant-iT PicoGreen dsDNA assay kit (ThermoFisher Scientific, USA) was employed to measure the DNA quantity by following the manufacturer's specifications. Additionally, the remaining GAGs and collagen components were detected by using the following kits: the Blycan™ sulfated glycosaminoglycans assay kit (Biocolor) and the collagen assay kit (Chondrex, Inc.). Histological staining with H&E and immunofluorescence staining with DAPI were used to visualize the remaining nuclei after decellularization, and images were visualized under a confocal fluorescent microscope (Olympus, FV10i-W, Tokyo, Japan). Further, the surface morphology of decellularized and native ECM was observed under scanning electron microscopy (SEM) (SEM, JEOL, JSM-6701F, Tokyo, Japan).

4.3. Sample preparation and LC-MS/MS analysis

The freeze-dried powdered tissue samples were collected and then suspended in 1 mL of lysis buffer (8 M urea–0.1 m Tris-HCl buffer, pH 8.5) and 40 μL of protease inhibitor cocktail (25 × stock), followed by sonication for 20–40 min at 15 °C using a Covaris S2 Focused-Ultrasonicator (Covaris, Woburn, MA, USA). The protein concentration was quantified using the Pierce BCA Protein Assay Kit (Thermo Fisher Scientific). Filter-Aided Sample Preparation (FASP) was then performed for the digestion step on a Microcon 30K centrifugal filter device (Millipore, Billerica, MA, USA). Each 100 μg of sample was reduced by incubating with TCEP at 37 °C for 30 min and then alkylated with iodoacetic acid at 25 °C in dark conditions for 1hr. After completing

the washing stage with lysis buffer and 50 mm Ammonium Bicarbonate, the proteins were digested with trypsin (enzyme to protein ratio of 1:50; w/w) at 37 °C for 18 h. Subsequently, in a new tube, the resulting peptide mixtures were transferred, and the trypsin was inactivated by acidifying with 15 μL of formic acid. Finally, the digested peptides were desalted using C18 spin columns (Harvard Apparatus, Holliston, MA, USA), and the peptides were eluted with 80 % acetonitrile in 0.1%formic acid (Honeywell, Charlotte, NC, USA) in distilled water.

For LC-MS/MS analysis, the prepared samples were resuspended in 0.1 % formic acid in water and analyzed using a Q-Exactive Orbitrap hybrid mass spectrometer (Thermo Fisher Scientific, Waltham, MA, USA) with an Ultimate3000 system (Thermo Fisher Scientific, Waltham, MA, USA). Depending on peptide hydrophobicity, a trap column packed with 3 μm C18 resin (2 cm × 75 μm ID) and an analytical column packed with 2 μm C18 resin (50 cm × 75 μm ID) were utilized. A data-dependent acquisition method was used and the top 10 precursor peaks were selected and isolated for fragmentation. Ions were scanned at high resolution (70000 in MS1, 17500 in MS2 at m/z 400), and for both the MS1 and MS2 levels, the MS scan range was set from 400 to 2000 m/z. Additionally, the precursor ions were fragmented with NCE (Normalized Collisional Energy) 27 % and 30s was set for the dynamic exclusion.

4.4. Proteome data analysis

Thermo Proteome Discoverer software (ver. 3.1) was used for the analysis of each Thermo MS/MS raw files, and the *Sus scrofa* database was used from UniProt. The analysis workflow included a peptide-spectrum match (PSM) validation step and utilized the SEQUEST HT as the database search algorithm. The search parameters were configured as follows: 10 ppm of tolerance of precursor ion masses, 0.02 Da fragment ion mass, and a maximum of two missed cleavages with trypsin enzyme. Dynamic modification of the peptide sequence was used as follows: static carbamidomethylation of cysteine (+57.012 Da), variable modifications of methionine oxidation (+15.995 Da), acetylation of protein N-term (+42.011 Da), and carbamylation of protein N-term (+43.0006 Da). Results with an FDR below 1 % were selected and filtered for peptides with at least 6 more peptide lengths.

The differentially expressed genes and the clustering heatmap analysis were performed by the Excel-based Differentially Expressed Gene analysis tool (ExDEGA) and ExDEGA Graphic Plus, where all genes with $P < 0.05$ and normalized data 4.00 log2 were considered to conduct the analysis. Moreover, differentially expressed genes with $P < 0.05$, FDR <0.25, and log2 fold change greater or less than ±2 were selected and uploaded to STRING for analysis of the functional protein association network and gene ontology enrichment analysis. Kyoto Encyclopedia of Genes and Genomes (KEGG) analysis was performed by selecting the genes with $P < 0.05$, FDR <0.25 and log2 fold change greater or less than ± 2 (www.kegg.jp) and plotting the graph using SRPLOT. KEGG analysis involves predicting manually curated pathway maps with significant genes to represent the hypotheses of molecular interaction and reaction networks in biological processes.

4.5. Preparation of TOCN

TOCN (Conc. 1 %) was obtained from the Korea Forest Institute, South Korea. It was prepared from softwood bleached kraft pulp by the TEMPO method. Briefly, cellulose (1.95 g, 12 mmol anhydroglucose units) was dispersed in distilled water using a highspeed homogenizer (M-110EH30, Microfluidics, USA). Subsequently, the cellulose solution was combined with a solution containing TEMPO (30 g, 0.19 mmol, Sigma Aldrich, USA), NaBr (0.63 g, 6.1 mmol; Sigma Aldrich, USA), and NaOCl (1.76 M solution, 15 mL, 2.64 mmol; Sigma Aldrich, USA) and stirred well until it dissolved appropriately. The pH of the solution was maintained at 10 by adding 0.5 M NaOH. Following this, the residual activity of NaOCl was neutralized by adding 5 mL methanol, and the pH was adjusted to 7 by adding 0.5 M HCl. The mixture was centrifuged to get the oxidized cellulose derivative and surface carboxylated cellulose nanocrystal pellets. To thoroughly purify the TOCN, the centrifugation and re-dispersion of cellulose derivatives were repeated 2–3 times, followed by dialysis against the distilled water. However, the specific oxidation degree of TOCN was not measured for this study.

4.6. Cell culture of ADSCs

Rabbit Adipose-derived stem cells (ADSCs) were isolated and cultured in a primary medium Dulbecco's modified Eagle's medium (DMEM) F-12 (WelGENE, Republic of Korea) containing 2 mg/ml collagenase I (Worthington, USA), 10 % FBS and 1 % penicillin-streptomycin (100 U/mL) in a humidified incubator at 37 °C with 5 % CO_2. The media was replaced 3 times per week. After the cell confluency reached 80%–90 %, the adherent cells were trypsinized, harvested, and further subcultured in other dishes. ADSCs passage 7 was used for the experiment in this study.

4.7. Preparation of stem cell-laden bio-ink

The natural bio-inks for 3D bio-printing were prepared by mixing dECM and TOCN, where the concentration of both dECM and TOCN was 1 %. Briefly, a 1:1 ratio of dECM and TOCN was thoroughly mixed, and then 4 % sodium alginate (SA) (Junsei, Japan) was directly added under continuous stirring until the alginate powder dissolved completely. The hydrogel was sterilized under UV light (254 nm) and loaded into a sterile syringe to crosslink with a sterile aqueous $CaCl_2$ solution (Samchun pure chemical) (3 % based on dry SA content) using a two-syringe coupler method. For 10 ml of bio-ink, 500 μl of $CaCl_2$ solution was employed for crosslinking. The mixing process was carried out back and forth slowly avoiding bubble formation and continued until it formed a paste hydrogel with appropriate elastic properties. After that, 200 μl of ADSCs (2×10^7) cell suspension loaded with 10 ng/ml TGFβ-1 (Peprotech, USA) and 20 ng/ml FGF-18 (Peprotech, USA) was mixed gradually with the hydrogel to prepare a stem cell-laden bio-ink. The optimum concentrations of the growth factors were chosen based on the published research [74,79,84]. All the process was performed under a clean bench in an aseptic condition to avoid contamination. Different bio-ink compositions are reported in Table 1.

4.8. Fabrication of 3D bio-printed scaffolds

The scaffolds were fabricated using 3D bio-printing technology following our previous study protocol [36]. Briefly, a stereolithography (STL) file of the 3D models of the scaffolds was designed using Autodesk Fusion 360 CAD software. Then, a 3D bio-plotter software was used to set the bio-printing parameters like printing speed, layer height, infill density, pore diameter between the layers, and infill pattern. Finally, the 3D model was sliced and translated into a G-Code file. Next, the 3D bioprinting was conducted at room temperature using a 3D bioprinter (Rokit Invivo, South Korea). Following bio-printing, the scaffolds were crosslinked immediately in 100 mM sterile $CaCl_2$ solution for 5 min, rinsed with sterile PBS, and incubated in a DMEM F-12 media containing 10 % FBS and 1 % penicillin-streptomycin (100 U/mL) at 37 °C with 5 % CO_2 for further experiments. All the bioprinting process parameters are displayed in Table S8.

4.9. Viscosity and printability of dECM/TOCN/alginate hydrogels

The viscosity of the hydrogels was assessed after partial crosslinking to evaluate their printability. Initially, viscoelastic behavior was measured by using a Brookfield viscometer (DV2T, USA) with spindle number SC4-27. The viscosity testing was conducted at various rpm and the temperature sensitivity test was performed from 25 °C to 36 °C under a low and high shear rate. The printability of the hydrogels was already performed in our previously published study [36]. However, in this

study, we tested again by extruding the gel through the bioprinter extruder and printing the scaffolds. As well as performing the viscosity with and without TOCN; the parameters are detailed in Table S9.

4.10. Fourier transform infrared spectroscopy (FT-IR)

Fourier Transform Infrared Spectroscopy (FT-IR) was conducted to identify the functional groups present in the different scaffolds. The chemical composition of the DTS, DTST, DTSF, and DTSTF was determined by Fourier transform infrared spectroscopy using a Nicolet spectrometer (Nicolet Ia10, Thermo Scientific). The samples were analyzed over the range of 4000-1000 cm^{-1} using OMNIC 7.3 spectra software.

4.11. Surface morphology and stem cell distribution analysis

The surface morphology of the scaffolds was examined by scanning electron microscopy (SEM, JEOL, JSM-6701F, 197 Tokyo, Japan). Briefly, the dried electrospun membranes were sectioned into small pieces and placed on the sample holder. Subsequently, the samples were coated with platinum using a sputter coater (Cressington Scientific Instrument, Watford, UK). Images were taken at an acceleration voltage of 10 kV.

4.12. Mechanical strength analysis

The compressive properties of the rectangular scaffolds were evaluated using a universal mechanical testing machine (UTM, Qmesys, QM100T). This testing machine was equipped with a 100 N load cell. In brief, the scaffolds were crosslinked in 100 mM CaCl2 solution for 10 min and rinsed with PBS. Then, the mechanical strength was measured by compressing the samples until they fragmented in a wet state at room temperature. Finally, the compressive Young's modulus was measured from the slope of the strain-stress curve. All the tests were performed in triplicates.

4.13. Water absorption and degradation behavior

The water absorption of the scaffolds was assessed by the conventional weighing method. Initially, each dry scaffold was first weighed (W0) and immersed in 2 mL PBS. The wet samples were then maintained in a 37 °C incubator. At specific time intervals (1 h, 12 h, and 24 h), the scaffolds were removed, and excess water was blotted with filter paper. Then, the wet weight (Wt) of each scaffold was recorded. Finally, the percent of water content was calculated as the following Eq. (1):

$$\text{Water content } (\%) = \frac{(Wt - Wo)}{Wo} \times 100 \quad (1)$$

where W0 is the initial dry weight and Wt is the wet weight of each sample at a different time point. Each sample was independently run in triplicates.

The degradation behavior of the samples was monitored over 28 days. Three specimens from each group were initially placed on separate Petri dishes and weighed to establish initial values for the degradation assessment. Subsequently, 5 mL of phosphate-buffered saline (PBS; pH 7.4) was added to each plate, and the samples were incubated on a reciprocal shaker (SH30L) at 37 °C. The PBS solution was refreshed daily to maintain a consistent environment. At designated time points 1, 4, 7, 14, 21, and 28 days the PBS was removed, and each sample was thoroughly washed. Following freeze drying, weight variations in the samples were noted. Then the samples were weighed (Wt) again to measure the percentage of degradation rate (%) according to the following equation (2):

$$\text{Degradation rate } (\%) = \frac{(Wo - Wt)}{Wo} \times 100 \quad (2)$$

Here equation (3) represents W_o as the initial weight and W_t as the measured weight at each time period. Each sample was run in triplicate, independently.

4.14. Release rate of TGFβ-1 and FGF-18 from the scaffold

The release rate of both TGFβ-1 and FGF-18 from the scaffold was measured by extracting the growth factor from the scaffold. Briefly, a known weight of the scaffolds was immersed in 5 ml of PBS solution into 48 well plates. At specific time points (1, 3, 5, 7, 14, and 21) 2 ml PBS was collected and replenished with 2 ml fresh PBS solution. The quantity of released growth factors from the scaffolds was analyzed by ELISA kit following the manufacturer's protocol. A standard calibration curve of TGFβ-1 and FGF-18 was employed to calculate the concentrations of the growth factor released. The percentage of growth factor released from the scaffolds was calculated based on the initial weight of the growth factor incorporated into the scaffolds.

4.15. Cytotoxicity and live/dead cell assay

In vitro, cytotoxicity of the different scaffolds was investigated by MTT assay using sample extract following the standard testing protocol. Briefly, after 3D bio-printing, the scaffolds were placed in 48-well plates (n = 3 per group). Where ADSCs at a density of (1×10^5) were printed with the scaffolds and incubated at 37 °C with 5 % CO2 for 1, 3, and 7 days. On a specific day, the MTT solution (1:10 ratio) was added to each well of the samples and incubated at 37 °C for 4 h. Finally, the solution was removed, and 400 μl of DMSO was added to each well and incubated for 30 min to solubilize the formazan crystals. The absorbance of the solutions (n = 3 each group) was measured using a microplate reader (Biotek, Synergy H1, USA) at a wavelength of 570 nm. The cell culture medium was replaced every 2 days.

The live/dead cell assay was conducted using a live/dead viability/cytotoxicity Kit (Thermofisher Scientific, USA) following the manufacturer's protocol. Briefly, after 3D bio-printing of the scaffolds with ADSCs cell suspension (1×10^6), the samples were cultured for 24 h at 37 °C with 5 % CO2. The staining solution was prepared with 5 μL calcein AM and 20 μL ethidium homodimer-1 in 10 mL PBS. At a specific time, point after removing the media, 100–200 μL of the staining solution was added directly to the cells in each well and incubated for 30 min at 20–25 °C. Then the live/dead cells were visualized and analyzed using a confocal fluorescent microscope (Olympus, FV10i-W, Tokyo, Japan). The live/dead cells were counted from the fluorescence images after 24 h of culture using Fiji software (National Institutes of Health (NIH), USA). The cell viability was calculated using the following formula (3):

$$\text{Cell viability } (\%) = \frac{\text{Total Cells} - \text{Dead Cells}}{\text{Total Cells}} \times 100 \quad (3)$$

4.16. Wound healing and transwell migration assay

The wound healing assay was performed by seeding the ADSCs (1×10^4 cells/well) in 6 well plates and culturing them at 37 °C with 5 % CO2. Briefly, the condition media were collected from different sample groups by immersing the sample membrane in a culture medium for 24 h at 37 °C. Once the ADSCs reached confluency, a liner wound was introduced by scraping ADSCs gently with a 200 μl pipette tip at the center of the well. After washing with PBS to remove the detached cells and other cellular debris, the conditioned media were added to each well of the different groups. Finally, images of the scratch were taken over a period of 0–24 h to determine the wound repair rate. The wound area was analyzed from the images using scratch assay analysis software (TScratch, CSElab). Each experiment was performed in triplicate, independently.

To compare the cell mobility between FGF-18 and TGFβ-1, a migration assay was performed with the Transwell system. Briefly, 2000

cells were seeded at the bottom of the upper chamber, and the lower chamber was filled with 500 μl DMEM and 0.5 % FBS, supplemented with FGF-18 (20 ng/ml) or TGFβ-1 (10 ng/ml). 8 h after seeding, the cells were fixed with 4 % PFA and stained with crystal violet for 10 min at room temperature. An optical microscope was used to analyze of cell migration assay. All the migrated cells were analyzed using Fiji software (National Institutes of Health (NIH), USA).

4.17. Chondrogenic differentiation

Chondrogenic differentiation was performed by centrifuging the ADSCs (3×10^7) and collecting them in 15 mL polypropylene tubes, followed by culturing for 21 days in a differentiation medium containing DMEM supplemented with 0.1 mM dexamethasone, 10 % FBS, 50 μg/mL l-ascorbic acid, 5 μg/mL ITS premix, 100 μg/mL sodium pyruvate, TGF-β1 (10 ng/mL), FGF-18 (20 ng/mL) and DTS extract. Cell pellets (n = 3) were collected on day 21 and fixed in 4 % paraformaldehyde overnight. After paraffin embedding and sectioning into 5 μm thick slices, the sections were stained with H&E, Safranin-O, and alcian blue to demonstrate chondrogenic differentiation. The sections were visualized under light microscopy (Olympus). Furthermore, RT-PCR gene expression analysis with SOX9 and immunofluorescence staining of COL2, ACAN, and PRG4 were performed. The experimental method of RT-PCR was provided in the supplementary section.

4.18. In vivo cartilage regeneration studies

Adult male New Zealand white rabbits weighing between 3.0 and 3.5 kg were used for the study *in vivo*. After receiving the animals were housed in standard cages with free access to equal amounts of food and water, according to the Animal Ethics Committee of Soonchunhyang University, South Korea (Number: SCH22-0071). All the experiments related to animals *in vivo* complied with the arrival guidelines and regulations. A total of 18 rabbits were designated for histological assessment and another 6 rabbits for MRI and mechanical assessment, and these were randomized into three groups: Control (Untreated), DTS, and DTSTF. Including additional groups, such as DTST and DTSF, in the *in vivo* study would have required a larger number of animals, raising ethical concerns and resource constraints. Therefore, we optimized our study approach to balance scientific rigor with ethical considerations. We started the surgery by giving the anesthesia, and then the knee joint of the rabbits was exposed after dislocating the patella. A cylindrical defect (4-mm diameter, 3-mm depth) on the trochlear groove of the distal femur was created using a corneal trephine and suitably matched 3D bioprinted scaffolds were implanted. Forced flexion and extension were performed for the operated knees to ensure the implanted scaffolds were correctly positioned within the defects. Lastly, the operated knee joints were closed with a suture (4-0 thread), and antibiotics were given intramuscularly for prophylactic infection. After the operation, rabbits were allowed to move freely in their single cages and fed with standard food and water. 3 months and 6 months later, rabbits were euthanized for further study.

4.19. Magnetic resonance imaging (MRI) analysis

The body temperature of the animals was maintained with a heating pad on the animal holder during MRI experiments. At 6 months post-surgery, each rabbit in the experimental groups underwent MRI analysis on a Siemens TIM Trio 3 T (T) MRI scanner (Siemens, Erlangen, Germany) equipped with a small animal-specific knee coil (Chenguang Medical Technologies Co., Ltd, Shanghai, China) to improve the signal-to-noise and contrast-to-noise ratios. The average acquisition time was approximately 35 min. T2 and T2* values were analyzed by a senior musculoskeletal radiologist using an inline processing package (Syngo-MapIt; Siemens). Finally, MicroDicom viewer was used to analyze the regenerated cartilage.

4.20. Biomechanical assessment of regenerated cartilage

Biomechanical analysis of tissue repair was conducted using nano-indentation with a TriboIndenter (Hysitron Inc., Minneapolis, MN, USA), equipped with a Berkovich tip with a 400-μm radius. To evaluate the mechanical properties of regenerated cartilage, distal femurs were extracted, and the posterior portions of the condyles were excised to yield tissues of consistent thickness. The remaining section, containing the defect in the trochlear groove, was firmly fixed onto a glass slide, covered with saline, and measured using a silicon nitride cantilever (k = 1.00 N/m) with a 12 μm diameter borosilicate glass bead (Novascan Technologies) attached. Three different regions (Fig. S8B) of each sample were assessed by applying a trapezoidal load function up to 5000 μN peak force to derive an average value; the loading time was 10s, the holding time 10s, and the unloading time 10s. Indentations were controlled by force up to a maximum depth of 1200 nm. Finally, the indentation depth, elastic modulus, and hardness of the examined regions were calculated and analyzed.

4.21. Micro CT analysis

The desired tissue sections were fixed using 4 % PFA. A micro-CT scanner (SkyScan 1172, Bruker, Belgium) was used to scan the fixed samples and assess the cartilage regeneration. The scanned data were reconstructed using NRecon software, and the regenerated cartilage and subchondral bone formation were investigated. Reconstructed images were imported and analyzed using CTAn (SkyScan) and CTVol (SkyScan) software.

4.22. Histological analysis

After 3 and 6 months of implantation, the knee joint was immediately fixed in 4 % PFA for 7 days and decalcified in 5 % nitric acid solution for 7 days. Subsequently, the samples were processed for paraffin embedding. The paraffin-embedded samples were sectioned at 5 μm thickness and stained with H&E, Safranin-O/Fast green, Masson's trichrome (MT), and Alcian blue/Nuclear fast red for immunohistological analysis. To evaluate the histological structure, a light microscope (Olympus, Japan) was used to observe the tissue sections, and the images were analyzed using cellSens software.

4.23. Immunofluorescence analysis

The expression profiles of the COL2 (Prosci, USA), ACAN (Thermofisher, USA), PRG4 (Sigma-Aldrich, USA), Smad4 (Bioss Inc., USA), and AKT (Antibodies-online, USA) were observed through immunofluorescence staining. Briefly, paraffin-embedded samples were permeabilized using 0.5 % Triton X-100. After washing the samples three times with PBS, they were then blocked with 10 % goat serum at room temperature for 50 min. Subsequently, the sections were incubated with the primary antibodies for COL2, ACAN, PRG4, Smad4, and AKT at 4 °C overnight. Following incubation, the samples underwent a triple wash with PBS, and then the sections were incubated with secondary antibody Alexa 488 anti-mouse (A12379, Thermo Fisher, US) in a dark chamber for 1 h at 37 °C. DAPI was employed for nuclear staining. After staining, the tissue sections were visualized using a light microscope (Olympus, Japan). The positively stained areas of the markers were quantitatively analyzed using Fiji software (National Institutes of Health (NIH), USA).

4.24. In silico protein-protein docking simulation analysis

The 3D structures of FGF-18 (PDB ID: 4cjm), FGF-R3 (PDB ID: 6lvm), TGFβ-1 (PDB ID: 3kfd), and TGFβ-R2 (PDB ID: 1ktz) were retrieved from the website of protein data bank (https://www.rcsb.org). All the proteins were processed by PyMOL software. Protein-protein docking analysis was performed by the ClusPro2.0 online docking server [105].

The ClusPro server offers numerous features for the editing of protein models and is widely applied in molecular docking. RasMol software was used to visualize the protein-docked models [106]. PDBsum (https://www.ebi.ac.uk/thornton-srv/databases/pdbsum/Generate.html) online server use employed to identify types of interaction of the amino acids between the two docked proteins.

4.25. Statistical analysis

Statistical analysis was conducted using t-tests, one-way variance (ANOVA), and two-way (ANOVA, Tukey test) analysis with GraphPad Prism 8.0. All the experiments were performed in triplicate, and the results were presented as the mean ± standard deviation (SD). The statistical significance was set as ns; no significant, *p < 0.05, **p < 0.01, ***p < 0.001, and ****p < 0.0001.

CRediT authorship contribution statement

Prayas Chakma Shanto: Writing – original draft, Visualization, Validation, Software, Methodology, Investigation, Formal analysis, Data curation, Conceptualization. **Seongsu Park:** Investigation, Data curation. **Md Abdullah Al Fahad:** Visualization, Validation, Software, Data curation. **Myeongki Park:** Data curation, Formal analysis, Investigation. **Byong-Taek Lee:** Writing – review & editing, Visualization, Validation, Supervision, Resources, Project administration, Funding acquisition.

Ethics approval and consent to participate

Adult male New Zealand white rabbits were housed in standard cages with free access to equal amounts of food and water, according to the Animal Ethics Committee of Soonchunhyang University, South Korea (Number: SCH22-0071). All the experiments related to animals *in vivo* complied with the arrival guidelines and regulations.

Declaration of competing interest

The authors declare that they have no conflict of interest.

Acknowledgments

This study was supported by the Basic Science Research Program through the National Research Foundation (NRF), funded by the Ministry of Education, Republic of Korea (2015R1A6A1A03032522), Technology Development Program (RS-2023-00281111) funded by the Ministry of SMEs and Startups (MSS, Korea) and partially funded by the Soonchunhyang University, Republic of Korea.

Appendix A. Supplementary data

Supplementary data to this article can be found online at https://doi.org/10.1016/j.bioactmat.2024.12.021.

References

[1] Y. Li, et al., O-alg-THAM/gel hydrogels functionalized with engineered microspheres based on mesenchymal stem cell secretion recruit endogenous stem cells for cartilage repair, Bioact. Mater. 28 (2023) 255–272.
[2] X. Guo, et al., Regeneration of articular cartilage defects: therapeutic strategies and perspectives, J. Tissue Eng. 14 (2023) 20417314231164765.
[3] D.J. Hunter, L. March, M. Chew, Osteoarthritis in 2020 and beyond: a lancet commission, Lancet 396 (10264) (2020) 1711–1712.
[4] N.K. Arden, et al., Non-surgical management of knee osteoarthritis: comparison of ESCEO and OARSI 2019 guidelines, Nat. Rev. Rheumatol. 17 (1) (2021) 59–66.
[5] K.A. Waller, et al., Role of lubricin and boundary lubrication in the prevention of chondrocyte apoptosis, Proc. Natl. Acad. Sci. USA 110 (15) (2013) 5852–5857.
[6] L. Zhou, et al., Engineered biochemical cues of regenerative biomaterials to enhance endogenous stem/progenitor cells (ESPCs)-mediated articular cartilage repair, Bioact. Mater. 26 (2023) 490–512.
[7] M. Wang, et al., Articular cartilage repair biomaterials: strategies and applications, Mater. Today Bio (2024) 100948.
[8] S.L. Ding, et al., Cartilage lacuna-inspired microcarriers drive hyaline neocartilage regeneration, Adv. Mater. 35 (30) (2023) 2212114.
[9] Z. Gu, et al., Smart biomaterials for articular cartilage repair and regeneration, Adv. Funct. Mater. 33 (10) (2023) 2212561.
[10] Y. Yang, et al., Ultra-durable cell-free bioactive hydrogel with fast shape memory and on-demand drug release for cartilage regeneration, Nat. Commun. 14 (1) (2023) 7771.
[11] Y. Hu, et al., Glycopolypeptide hydrogels with adjustable enzyme-triggered degradation: a novel proteoglycans analogue to repair articular-cartilage defects, Mater. Today Bio 20 (2023) 100659.
[12] X. Ding, et al., Synthetic peptide hydrogels as 3D scaffolds for tissue engineering, Adv. Drug Deliv. Rev. 160 (2020) 78–104.
[13] O. Jeznach, D. Kołbuk, P. Sajkiewicz, Injectable hydrogels and nanocomposite hydrogels for cartilage regeneration, J. Biomed. Mater. Res. 106 (10) (2018) 2762–2776.
[14] J. Maihöfer, et al., Hydrogel-guided, rAAV-mediated igf-I overexpression enables long-term cartilage repair and protection against perifocal osteoarthritis in a large-animal full-thickness chondral defect model at one year in vivo, Adv. Mater. 33 (16) (2021) 2008451.
[15] C. Shen, et al., Boosting cartilage repair with silk fibroin-DNA hydrogel-based cartilage organoid precursor, Bioact. Mater. 35 (2024) 429–444.
[16] Z. Zhou, et al., Dual-network DNA–silk fibroin hydrogels with controllable surface rigidity for regulating chondrogenic differentiation, Mater. Horiz. 11 (6) (2024) 1465–1483.
[17] T.Z. Li, et al., Using cartilage extracellular matrix (CECM) membrane to enhance the reparability of the bone marrow stimulation technique for articular cartilage defect in canine model, Adv. Funct. Mater. 22 (20) (2012) 4292–4300.
[18] M.P. Murphy, et al., Articular cartilage regeneration by activated skeletal stem cells, Nat. Med. 26 (10) (2020) 1583–1592.
[19] K. Johnson, A stem cell-based approach to cartilage repair, Osteoarthritis Cartilage 21 (2013) S4.
[20] X. Liu, et al., Molecular recognition-directed site-specific release of stem cell differentiation inducers for enhanced joint repair, Biomaterials 232 (2020) 119644.
[21] X. Li, et al., Research progress in hydrogels for cartilage organoids, Adv. Healthcare Mater. (2024) 2400431.
[22] T.P. Nguyen, et al., Cell-laden injectable microgels: current status and future prospects for cartilage regeneration, Biomaterials 279 (2021) 121214.
[23] S. Yin, Y. Cao, Hydrogels for large-scale expansion of stem cells, Acta Biomater. 128 (2021) 1–20.
[24] H. Xuan, et al., Biofunctionalized chondrogenic shape-memory ternary scaffolds for efficient cell-free cartilage regeneration, Acta Biomater. 105 (2020) 97–110.
[25] A. Dufour, et al., Integrating melt electrowriting and inkjet bioprinting for engineering structurally organized articular cartilage, Biomaterials 283 (2022) 121405.
[26] P. Abdollahiyan, et al., Hydrogel-based 3D bioprinting for bone and cartilage tissue engineering, Biotechnol. J. 15 (12) (2020) 2000095.
[27] F. Gao, et al., Osteochondral regeneration with 3D-printed biodegradable high-strength supramolecular polymer reinforced-gelatin hydrogel scaffolds, Adv. Sci. 6 (15) (2019) 1900867.
[28] S.H. Kim, et al., Precisely printable and biocompatible silk fibroin bioink for digital light processing 3D printing, Nat. Commun. 9 (1) (2018) 1620.
[29] C. Qin, et al., 3D bioprinting of multicellular scaffolds for osteochondral regeneration, Mater. Today 49 (2021) 68–84.
[30] D. Wu, et al., Enhanced osteochondral regeneration with a 3D-Printed biomimetic scaffold featuring a calcified interfacial layer, Bioact. Mater. 36 (2024) 317–329.
[31] Q. Yao, et al., Chondrogenic regeneration using bone marrow clots and a porous polycaprolactone-hydroxyapatite scaffold by three-dimensional printing, Tissue Eng. 21 (7–8) (2015) 1388–1397.
[32] W. Shi, et al., Structurally and functionally optimized silk-fibroin–gelatin scaffold using 3D printing to repair cartilage injury in vitro and in vivo, Adv. Mater. 29 (29) (2017) 1701089.
[33] J. Zhu, et al., Advanced application of collagen-based biomaterials in tissue repair and restoration, J. Leather Sci. Eng. 4 (1) (2022) 30.
[34] Y. Liu, et al., 3D-bioprinted BMSC-laden biomimetic multiphasic scaffolds for efficient repair of osteochondral defects in an osteoarthritic rat model, Biomaterials 279 (2021) 121216.
[35] F. Pati, et al., Printing three-dimensional tissue analogues with decellularized extracellular matrix bioink, Nat. Commun. 5 (1) (2014) 3935.
[36] P.C. Shanto, et al., Physico-biological evaluation of 3D printed dECM/TOCN/alginate hydrogel based scaffolds for cartilage tissue regeneration, Biomater. Adv. (2022) 213239.
[37] Kim, Y.-H., et al., Human bone tissue-derived ECM hydrogels: controlling physicochemical, biochemical, and biological properties through processing parameters. Bioact. Mater., 2025. 43: p. 114-128.
[38] G. Chinga-Carrasco, Potential and limitations of nanocelluloses as components in biocomposite inks for three-dimensional bioprinting and for biomedical devices, Biomacromolecules 19 (3) (2018) 701–711.
[39] B.A. de Melo, et al., 3D printed cartilage-like tissue constructs with spatially controlled mechanical properties, Adv. Funct. Mater. 29 (51) (2019) 1906330.
[40] Y. Meng, et al., 3D printing of a poly (vinyl alcohol)-based nano-composite hydrogel as an artificial cartilage replacement and the improvement mechanism of printing accuracy, J. Mater. Chem. B 8 (4) (2020) 677–690.

[41] R. Schipani, et al., Reinforcing interpenetrating network hydrogels with 3D printed polymer networks to engineer cartilage mimetic composites, Biofabrication 12 (3) (2020) 035011.
[42] C. Antich, et al., Bio-inspired hydrogel composed of hyaluronic acid and alginate as a potential bioink for 3D bioprinting of articular cartilage engineering constructs, Acta Biomater. 106 (2020) 114–123.
[43] M. Di Giuseppe, et al., Mechanical behaviour of alginate-gelatin hydrogels for 3D bioprinting, J. Mech. Behav. Biomed. Mater. 79 (2018) 150–157.
[44] C.R. Harrell, et al., Mesenchymal stem cell-based therapy of osteoarthritis: current knowledge and future perspectives, Biomed. Pharmacother. 109 (2019) 2318–2326.
[45] I. Grafe, et al., TGF-β family signaling in mesenchymal differentiation, Cold Spring Harbor Perspect. Biol. 10 (5) (2018) a022202.
[46] Q.O. Tang, et al., TGF-β3: a potential biological therapy for enhancing chondrogenesis, Expet Opin. Biol. Ther. 9 (6) (2009) 689–701.
[47] C. Cicione, et al., Alternative protocols to induce chondrogenic differentiation: transforming growth factor-β superfamily, Cell Tissue Bank. 16 (2015) 195–207.
[48] Q. Guo, et al., Dynamic proteinaceous hydrogel enables in-situ recruitment of endogenous TGF-β1 and stem cells for cartilage regeneration, Adv. Funct. Mater. (2024) 2403055.
[49] Y.I. Kim, et al., Overexpression of TGF-β1 enhances chondrogenic differentiation and proliferation of human synovium-derived stem cells, Biochem. Biophys. Res. Commun. 450 (4) (2014) 1593–1599.
[50] J. Ying, et al., Transforming growth factor-beta1 promotes articular cartilage repair through canonical Smad and Hippo pathways in bone mesenchymal stem cells, Life Sci. 192 (2018) 84–90.
[51] A. Mehlhorn, et al., Differential effects of BMP-2 and TGF-β1 on chondrogenic differentiation of adipose derived stem cells, Cell Prolif. 40 (6) (2007) 809–823.
[52] D. Davidson, et al., Fibroblast growth factor (FGF) 18 signals through FGF receptor 3 to promote chondrogenesis, J. Biol. Chem. 280 (21) (2005) 20509–20515.
[53] M. Chen, et al., Injectable microgels with hybrid exosomes of chondrocyte-targeted FGF18 gene-editing and self-renewable lubrication for osteoarthritis therapy, Adv. Mater. (2024) 2312559.
[54] B.P. Antunes, et al., Enhanced chondrogenic phenotype of primary bovine articular chondrocytes in Fibrin-Hyaluronan hydrogel by multi-axial mechanical loading and FGF18, Acta Biomater. 105 (2020) 170–179.
[55] C. Shu, et al., Use of FGF-2 and FGF-18 to direct bone marrow stromal stem cells to chondrogenic and osteogenic lineages, Future science OA 2 (4) (2016) FSO142.
[56] D. Correa, et al., Sequential exposure to fibroblast growth factors (FGF) 2, 9 and 18 enhances hMSC chondrogenic differentiation, Osteoarthritis Cartilage 23 (3) (2015) 443–453.
[57] G.S. Hussey, J.L. Dziki, S.F. Badylak, Extracellular matrix-based materials for regenerative medicine, Nat. Rev. Mater. 3 (7) (2018) 159–173.
[58] P. Panwar, et al., Aging-associated modifications of collagen affect its degradation by matrix metalloproteinases, Matrix Biol. 65 (2018) 30–44.
[59] D.M. Ornitz, P.J. Marie, Fibroblast growth factor signaling in skeletal development and disease, Gene Dev. 29 (14) (2015) 1463–1486.
[60] H. Chen, et al., Molecular mechanisms of chondrocyte proliferation and differentiation, Front. Cell Dev. Biol. 9 (2021) 664168.
[61] W. Chen, et al., 3D printing electrospinning fiber-reinforced decellularized extracellular matrix for cartilage regeneration, Chem. Eng. J. 382 (2020) 122986.
[62] Y. Wu, et al., 3D bioprinting of liver-mimetic construct with alginate/cellulose nanocrystal hybrid bioink, Bioprinting 9 (2018) 1–6.
[63] T. Sultana, J.-G. Gwon, B.-T. Lee, Thermal stimuli-responsive hyaluronic acid loaded cellulose based physical hydrogel for post-surgical de novo peritoneal adhesion prevention, Mater. Sci. Eng. C 110 (2020) 110661.
[64] H. Van Ho, et al., Novel TOCNF reinforced injectable alginate/β-tricalcium phosphate microspheres for bone regeneration, Mater. Des. 194 (2020) 108892.
[65] W. Hu, et al., Advances in crosslinking strategies of biomedical hydrogels, Biomater. Sci. 7 (3) (2019) 843–855.
[66] P.C. Shanto, et al., Multi-functional dual-layer nanofibrous membrane for prevention of postoperative pancreatic leakage, Biomaterials (2024) 122508.
[67] M. Mohamadhoseini, Z. Mohamadnia, Alginate-based self-healing hydrogels assembled by dual cross-linking strategy: fabrication and evaluation of mechanical properties, Int. J. Biol. Macromol. 191 (2021) 139–151.
[68] R. Karyappa, et al., Newtonian liquid-assisted material extrusion 3D printing: progress, challenges and future perspectives, Addit. Manuf. (2023) 103903.
[69] B. Luo, et al., An encapsulation-free and hierarchical porous triboelectric scaffold with dynamic hydrophilicity for efficient cartilage regeneration, Adv. Mater. (2024) 2401009.
[70] S. Bhaladhare, S. Bhattacharjee, Chemical, physical, and biological stimuli-responsive nanogels for biomedical applications (mechanisms, concepts, and advancements): a review, Int. J. Biol. Macromol. 226 (2023) 535–553.
[71] Q. Wang, et al., Controlled synthesis of sodium alginate electrospun nanofiber membranes for multi-occasion adsorption and separation of methylene blue, Carbohydr. Polym. 205 (2019) 125–134.
[72] S.R. Caliari, J.A. Burdick, A practical guide to hydrogels for cell culture, Nat. Methods 13 (5) (2016) 405–414.
[73] Y. Mori, et al., Identification of fibroblast growth factor-18 as a molecule to protect adult articular cartilage by gene expression profiling, J. Biol. Chem. 289 (14) (2014) 10192–10200.
[74] E. Moore, et al., Fibroblast growth factor-18 stimulates chondrogenesis and cartilage repair in a rat model of injury-induced osteoarthritis, Osteoarthritis Cartilage 13 (7) (2005) 623–631.
[75] F. Yin, et al., Cartilage regeneration of adipose-derived stem cells in the TGF-β1-immobilized PLGA-gelatin scaffold, Stem cell reviews and reports 11 (2015) 453–459.
[76] B. Xie, et al., Development and evaluation of 3D composite scaffolds with piezoelectricity and biofactor synergy for enhanced articular cartilage regeneration, J. Mater. Chem. B 12 (40) (2024) 10416–10433.
[77] N.N. DePhillipo, et al., Preclinical use of FGF-18 augmentation for improving cartilage healing following surgical repair: a systematic review, Cartilage 14 (1) (2023) 59–66.
[78] Y. Xie, et al., Fibroblast growth factor signalling in osteoarthritis and cartilage repair, Nat. Rev. Rheumatol. 16 (10) (2020) 547–564.
[79] X. Yao, et al., Fibroblast growth factor 18 exerts anti-osteoarthritic effects through PI3K-AKT signaling and mitochondrial fusion and fission, Pharmacol. Res. 139 (2019) 314–324.
[80] E.C. Lien, C.C. Dibble, A. Toker, PI3K signaling in cancer: beyond AKT, Curr. Opin. Cell Biol. 45 (2017) 62–71.
[81] H.-Q. Xu, et al., A review on cell damage, viability, and functionality during 3D bioprinting, Military Med. Res. 9 (1) (2022) 70.
[82] P. Shi, A. Laude, W.Y. Yeong, Investigation of cell viability and morphology in 3D bio-printed alginate constructs with tunable stiffness, J. Biomed. Mater. Res., Part A 105 (4) (2017) 1009–1018.
[83] N. Soltan, et al., Printability and cell viability in bioprinting alginate dialdehyde-gelatin scaffolds, ACS Biomater. Sci. Eng. 5 (6) (2019) 2976–2987.
[84] E. Music, et al., Transforming growth factor-beta stimulates human bone marrow-derived mesenchymal stem/stromal cell chondrogenesis more so than kartogenin, Sci. Rep. 10 (1) (2020) 8340.
[85] T. Vinikoor, et al., Injectable and biodegradable piezoelectric hydrogel for osteoarthritis treatment, Nat. Commun. 14 (1) (2023) 6257.
[86] K. Futrega, et al., A single day of TGF-β1 exposure activates chondrogenic and hypertrophic differentiation pathways in bone marrow-derived stromal cells, Commun. Biol. 4 (1) (2021) 1–12.
[87] L. Huang, et al., Synergistic effects of FGF-18 and TGF-β3 on the chondrogenesis of human adipose-derived mesenchymal stem cells in the pellet culture, Stem Cell. Int. (2018) 2018.
[88] J. Lin, et al., Research progress on injectable microspheres as new strategies for the treatment of osteoarthritis through promotion of cartilage repair, Adv. Funct. Mater. (2024) 2400585.
[89] H. Li, et al., Cartilage lacuna-biomimetic hydrogel microspheres endowed with integrated biological signal boost endogenous articular cartilage regeneration, Bioact. Mater. 41 (2024) 61–82.
[90] Y. Sun, et al., 3D bioprinting dual-factor releasing and gradient-structured constructs ready to implant for anisotropic cartilage regeneration, Sci. Adv. 6 (37) (2020) eaay1422.
[91] Z. Yang, et al., 3D-bioprinted difunctional scaffold for in situ cartilage regeneration based on aptamer-directed cell recruitment and growth factor-enhanced cell chondrogenesis, ACS Appl. Mater. Interfaces 13 (20) (2021) 23369–23383.
[92] L. Jia, et al., Bioprinting and regeneration of auricular cartilage using a bioactive bioink based on microporous photocrosslinkable acellular cartilage matrix, Bioact. Mater. 16 (2022) 66–81.
[93] Q. Li, et al., 3D printed silk-gelatin hydrogel scaffold with different porous structure and cell seeding strategy for cartilage regeneration, Bioact. Mater. 6 (10) (2021) 3396–3410.
[94] Chen, J., et al., Injectable acellular matrix microgel assembly with stem cell recruitment and chondrogenic differentiation functions promotes microfracture-based articular cartilage regeneration. Bioact. Mater., 2025. 44: p. 220-235.
[95] M. Morikawa, R. Derynck, K. Miyazono, TGF-β and the TGF-β family: context-dependent roles in cell and tissue physiology, Cold Spring Harbor Perspect. Biol. 8 (5) (2016) a021873.
[96] C. Cherifi, S. Monteagudo, R.J. Lories, Promising targets for therapy of osteoarthritis: a review on the Wnt and TGF-β signalling pathways, Ther. Adv. Muscul. Dis. 13 (2021) 1759720X211006959.
[97] C. Bauge, et al., Regulation and role of TGFβ signaling pathway in aging and osteoarthritis joints, Aging Dis. 5 (6) (2013) 394.
[98] P. Van der Kraan, et al., TGF-beta signaling in chondrocyte terminal differentiation and osteoarthritis: modulation and integration of signaling pathways through receptor-Smads, Osteoarthritis Cartilage 17 (12) (2009) 1539–1545.
[99] T.-F. Li, R.J. O'Keefe, D. Chen, TGF-β signaling in chondrocytes, Front. Biosci.: J. Vis. Literacy 10 (2005) 681.
[100] J. Ellsworth, et al., Fibroblast growth factor-18 is a trophic factor for mature chondrocytes and their progenitors, Osteoarthritis Cartilage 10 (4) (2002) 308–320.
[101] A. Gigout, et al., Sprifermin (rhFGF18) enables proliferation of chondrocytes producing a hyaline cartilage matrix, Osteoarthritis Cartilage 25 (11) (2017) 1858–1867.
[102] C.Y. Chuang, et al., Heparan sulfate-dependent signaling of fibroblast growth factor 18 by chondrocyte-derived perlecan, Biochemistry 49 (26) (2010) 5524–5532.
[103] L. Cinque, et al., FGF signalling regulates bone growth through autophagy, Nature 528 (7581) (2015) 272–275.

[104] K. Kita, et al., PI3K/Akt signaling as a key regulatory pathway for chondrocyte terminal differentiation, Gene Cell. 13 (8) (2008) 839–850.
[105] D. Kozakov, et al., The ClusPro web server for protein–protein docking, Nat. Protoc. 12 (2) (2017) 255–278.
[106] R.A. Sayle, E.J. Milner-White, RASMOL: biomolecular graphics for all, Trends Biochem. Sci. 20 (9) (1995) 374–376.